Title

A highly resolved integrated transcriptomic atlas of human breast cancers

Authors

Andrew Chen[1,2], Lina Kroehling[1,2], Christina S. Ennis[3], Gerald V. Denis[3,4,5], Stefano Monti[1,2,6]

Affiliations

1. Section of Computational Biomedicine, Boston University Chobanian and Avesidian School of Medicine, Boston, MA 02118, USA.
2. Bioinformatics Program, Center for Computing & Data Sciences, Boston University, Boston, MA 022158, USA.
3. Boston University-Boston Medical Center Cancer Center, Boston University Chobanian and Avesidian School of Medicine, Boston, MA, 02118, USA
4. Section of Hematology and Medical Oncology, Department of Medicine, Boston University Chobanian and Avesidian School of Medicine and Boston Medical Center, Boston, MA, 02118, USA
5. Department of Pharmacology and Experimental Therapeutics, Boston University Chobanian and Avesidian School of Medicine, Boston, MA, 02118, USA
6. Department of Biostatistics, Boston University School of Public Health, Boston, MA 02118, USA.
corresponding author(s): Stefano Monti (smonti@bu.edu)

Abstract

In this study, we developed an integrated single cell transcriptomic (scRNAseq) atlas of human breast cancer (BC), the largest resource of its kind, totaling > 600,000 cells across 138 patients. Rigorous integration and annotation of publicly available scRNAseq data enabled a highly resolved characterization of epithelial, immune, and stromal heterogeneity within the tumor microenvironment (TME). Within the immune compartment we were able to characterize heterogeneity of CD4, CD8 T cells and macrophage subpopulations. Within the stromal compartment, subpopulations of endothelial cells (ECs) and cancer associated fibroblasts (CAFs) were resolved. Within the cancer epithelial compartment, we characterized the functional heterogeneity of cells across the axes of stemness, epithelial-mesenchymal plasticity, and canonical cancer pathways. Across all subpopulations observed in the TME, we performed a multi-resolution survival analysis to identify epithelial cell states and immune cell types which conferred a survival advantage in both The Cancer Genome Atlas (TCGA) and METABRIC. We also identified robust associations between TME composition and clinical phenotypes such as tumor subtype and grade that were not discernible when the analysis was limited to individual datasets, highlighting the need for atlas-based analyses. This atlas represents a valuable resource for further high-resolution analyses of TME heterogeneity within BC.

Introduction

Breast cancer (BC) is the most prevalent cancer and the second most common cause of cancer death in women [1]. It is defined as a malignancy of the epithelial duct in breast tissue, and is a highly heterogeneous disease [2,3] for which clinical outcomes and responsiveness to treatment depend greatly on intrinsic factors related to the cancer cell, as well as extrinsic factors related to altered states of immune and stromal cells in the tumor microenvironment (TME) [4–6]. To improve our understanding of breast cancer progression and treatment, an extensive characterization of the heterogeneity in BC cancer cells and the surrounding tumor microenvironment is required.

Single cell transcriptomics (scRNAseq) remains the method of choice to characterize heterogeneity in tissue composition in terms of cell *types* – categories of cells that perform consistent functions, and in terms of cell *states* – categories of transient functions that can be shared across different cell types [7,8]. The technology has been extensively applied to profile healthy breast tissue, as part of the larger human cell atlas effort. There are now highly-resolved scRNAseq atlases that have annotated 700,000-800,000 cells across 55-126 samples yielding new insights into the diversity of immune, stromal, and epithelial populations in healthy breast tissue and how these are linked to clinical metadata [9,10]. However, the application of scRNAseq to profile breast cancer (BC) samples has been limited by cohort sizes, with most studies having fewer than 30 samples [11–20]. While these individual studies have laid substantial groundwork in characterizing tumor heterogeneity within BC, their limited sample size poses a challenge with reproducibility and identifying statistically significant associations between tissue composition and clinical metadata.

To address this challenge, we integrated eight publicly available scRNAseq datasets of untreated and unsorted BC samples [11–20] to create an atlas of transcriptional heterogeneity in BC. The analysis of this combined atlas enabled 1) the reconciliation of mislabeled cell types, 2) the identification of novel cell types, and 3) the association of changes in TME heterogeneity with clinical phenotypes such as tumor subtype and grade with increased statistical power (Fig 1a). Another study has attempted to integrate publicly-available scRNAseq BC data to create an atlas but compared to Xu et al. our study only contains unsorted BC samples, allowing for an unbiased characterization of inter-patient heterogeneity, and our atlas has a much a larger sample size (> 600,000 cells), enabling more robust identification of cell types and differentially abundant populations across phenotypes [21].

This integrated scRNAseq atlas provides an unbiased reference landscape of transcriptional heterogeneity in BC, comprised of more than 600,000 cells across 138 patients, the largest of its kind, and represents a valuable resource for hypothesis-driven analysis of TME heterogeneity. The data and methods described herein provide a robust framework for updating this BC atlas as new datasets are made publicly available [22].

Results

Constructing the integrated core atlas

The BC atlas was constructed by integrating eight publicly available scRNAseq datasets of untreated primary BC tumors. Across the eight datasets, samples were sequenced at varying throughput levels, and had different distributions of clinical and patient metadata including subtype, grade, and age (Fig. 1b,c,d). Before integration, batch effects were evident as cells separated by dataset of origin, rather than by biological factors (Supp Fig. 1). Six different integration approaches were applied and the best-performing method, as determined by atlas integration batch correction metrics [23] was Seurat's reciprocal PCA method (RPCA) (Fig 2a).

Relabeling of broad cell types

To annotate cells in the integrated atlas, we first defined three compartments: epithelial, immune, and stromal, by cross-referencing annotations from SingleR, CellTypist, and author annotations with broad clustering (Louvain clustering with resolution 0.1) (Supp Fig. 2). The resulting compartments showed distinct expression of canonical marker genes (Epithelial: *EPCAM, KRT8, KRT18*; Immune: *PTPRC, CD3D, CD3E, CD68*; Stromal: *COL1A1, COL1A2, ENG*) and diverse representation across all eight source datasets (Fig. 2b,c,d). More than 300,000 cells that previously had no available cell type annotation were annotated using the cluster-based annotations from the atlas (Fig. 2e).

These annotations of broad cell types based on integrated data also resulted in a relabeling of broad cell types for over 9172 cells (around 1% of the atlas) across 5 datasets (e.g., relabeling a cell as stromal that was originally labeled immune).

Cancer Epithelial Diversity

Intra-tumor heterogeneity within cancer cells stems from multiple factors including but not limited to genomic instability, epigenetic alterations, and clonal evolution which are all implicated in the treatment of cancer [24]. In this BC atlas, we sought to characterize intra and inter-tumor transcriptional heterogeneity by scoring each cancer cell with respect to potency/stemness [25], epithelial-mesenchymal plasticity (EMP) [26], malignancy [27], 'activity' of hallmark pathways [28], expression of epithelial cell type markers from HBCA [10], as well as clinical metadata related to age, tumor grade, and subtype (Fig. 3a). Further, we sought to find the driving factors of variation by leveraging a recursive partitioning tree-based method *K2 Taxonomer* [29] to identify meta-clusters and hierarchical relationships between them (Fig. 3b), and also trained random forests to extract the most discriminative features distinguishing each cluster and meta-cluster (Fig. 3c).

To identify functional groups of cancer cells shared across patients in the atlas, we performed unsupervised clustering (Louvain clustering with resolution 0.1) of cancer epithelial cells and identified 23 clusters that largely stratified by cell typist annotation based on the healthy Human Breast Cell Atlas (HBCA), author subtype, and Pam50 inferred subtype (Supp Fig. 3a,b,c,d). The differentially expressed genes for each epithelial cluster were identified using MAST (Supp Table 1). Several resolution parameters were evaluated (0.1-1.0) with even the coarsest resolution of 0.1 yielding multiple clusters (7,9,10,11,12,19,21) mostly consisting of cells from individual patients, as also revealed by their lowest entropy of donor proportions (Supp Fig. 3e,f). This suggests that the variation captured within these clusters was mostly driven by tumor-specific clonal expansion and, given our goal of defining shared programs of cancer epithelial heterogeneity, they were excluded from further downstream characterization.

<u>Multi-resolution characterization of cancer epithelial cells</u>

Among the remaining 16 epithelial clusters we identified the driving factors of variation within our cancer epithelial compartment by training random forest based classifiers at three separate levels of taxonomic resolution (Fig. 3b,c). In previous integrated single cell studies of breast cancer, cancer epithelial heterogeneity was characterized with respect to pam50 and clinical subtypes[11,12], as well as functional annotations by, e.g., Hallmark signatures [21], but has not yet been done in a hierarchical manner to identify the driving factors of variation.

This multi-level characterization revealed segregation of cancer epithelial cells at the highest level (Level 1) by stemness, EMP, and basal phenotypes, with clusters 13 through 4 (13~4) on the right side of the dendrogram exhibiting more stemness, more EMP (more mesenchymal),

and being more basal-like compared to clusters on the left side (clusters 0~16). At the next level of the dendrogram (Level 2), cancer cells on both sides segregated by age, with the left branch of the tree (clusters 0~16) segregating by older donors (clusters 0~20, 8, and 15~16) and younger donors (clusters 1~5), and the right branch of the tree (clusters 13~4) segregating by older (cluster 4) and younger (clusters 13~2) patients. At the next level of characterization (Level 3), finer groups of cancer epithelial heterogeneity emerge with clusters exhibiting decreased mitotic spindle activity (cluster 0), decreased TNFA signaling (cluster 20), increased EMT activity (cluster 13), as well as subtype-specific clustering (Luminal A: 1~17, 18; Luminal B: 6, 5, 15, 16; HER2: 3, 14), and grade specific clustering (high grade tumors: 8; low grade tumors: 6, 5, 18).

Immune and Stromal Cell Diversity in the TME

Across the immune and stromal compartments of the atlas, 20 immune and 14 stromal subpopulations were characterized (Fig. 4a,5a). These subpopulations were identified by integrating data from automatic annotation methods: SingleR [30] and CellTypist [31] (Supp Fig. 4,5), hierarchical tree-based methods (K2 Taxonomer) [29] (Fig. 4b, 5b), as well as marker genes obtained from differential expression analysis (MAST) [32] (Supp Table 2,3).

Reconciliation of immune cell subtypes to pan-cancer subtypes

Macrophages formed three clusters, which were all found to have analogs in previous pan-cancer and breast cancer specific characterizations of myeloid cells [10,33]. These included a cluster of lipid-associated macrophages *Mac. Lipo* defined by high expression of genes associated with lipid transport and metabolism (*LIPA, LPL, APOE, APOC1*); a cluster characterized by high expression of *MIK67* and *TOP2A* indicating a more proliferative state (*Mac Prolif)*; and a cluster of macrophages *Mac. Col* defined by strong expression of collagen genes (*COL1A1, COL1A2, COL3A1*), a subtype that has been previously been connected to ECM remodeling [34] (Fig. 4a,b,c).

T cells formed nine clusters (Fig. 4a), which were also found to have analogs in previous pan-cancer studies [13,35,36]. These included CD4 and CD8 effector memory T cells (*CD4/CD8 Tem*), which are characterized by expression of *LMNA, FOS,* and *GZMK, EOMES* respectively; CD4 Tregs defined by expression of *FOXP3, IL2RA,* and *TNFRSF4*; an interferon stimulated group of CD8 T cells (*CD8 ISG*) defined by strong expression of interferon signaling genes *IFIT1, IFIT2, IFIT3*; naïve CD4 cells characterized by expression of *CCR7, PASK, LEF1*; exhausted CD4 T cells (*CD4 Ex*) defined by expression of canonical exhaustion markers such as *LAG3, HAVCR2, PDCD1* and *TIGIT*; CD4 T follicular helper cells (*CD4 Tfh*) expressing transcription factors *TOX, TOX2* and chemokine *CXCL13*; CD4 T helper cells (*CD4 Th*) which in comparison to *CD4 Tfh* cells expressed high levels of interleukin genes *IL7R*, as well as the chemokine receptor *CCR6*. Similar to the macrophages, a proliferative T cell cluster (*T. Prolif*) was identified exhibiting strong expression of *MIK67* and *STMN1* (Fig. 4,a,b,d).

NK cells formed one cluster (Fig. 4a,d), which was defined by expression of Killer Cell Lectin receptors (*KLRD1, KLRF1*) and growth factor *FGFBP2*. A previous single cell breast cancer atlas identified 6 NK subtypes, although their atlas only contained 3720 NK cells across all studies, whereas our study identified one cluster with no discernable functional differences across a population of 23508 NK cells. This discrepancy may be attributed to the difference in sample size and clustering strategies between the two atlases [37].

Mast cells formed one cluster (Fig. 4a,c), defined by expression of the enzymes *TPSB2, CPA3,* and *TPSAB1*.

B Cells also formed a single cluster defined by canonical B cell markers such as *CD19*, *MS4A1*, *CD74* as well as expression of human leukocyte antigen genes such as *HLA-DRA* and *HLA-DPB1* (Fig. 4a,d).

Identification of dendritic subtypes

Dendritic cells formed four clusters (Fig. 4a,c), which include two conventional dendritic cell populations, one characterized by expression of *CLEC9A* (*cDC1*), and another characterized by expression of *CD1C* and *CLEC10A* (*cDC2*); a mature dendritic cell population (*mDC*) defined by *CCL22*, *CCR7*, and *CCL19* expression; and a plasmacytoid dendritic cell population (*pDC*) defined by expression of *GZMB*, *JCHAIN*, and *PTGDS*.

Reconciliation of stromal cell subtypes to pan-cancer subtypes

Fibroblasts formed six clusters (Fig. 5a,b,c), which were also reconciled to previously characterized pan-cancer stromal subtypes [38]. This includes five clusters of cancer-associated fibroblasts (CAFs) consisting of a population of *COL11A1+ CAFs* (*COL11A1*, *COL8A2*) implicated in collagen metabolism [38], a population of *LAMP5 CAFs* defined by expression of *LAMP5* and cystatins *CST1* and *CST2* implicated in promoting EMT [38], a population of PI16+ CAFs defined by expression of *PI16* and *PCOLCE2*, a population of DPT+ CAFs defined by expression of *DPT* and *CAPN6*, as well as population of CA12+ CAFs defined by expression of *CA12* and *SLC2A1* which has been implicated in glycolysis metabolism and hypoxia [38]. Apart from these CAFs subtypes, myofibroblasts also formed one cluster by expression of *RGS5* and *CDH6*.

Endothelial cells (ECs) surround blood vessels in the TME which are responsible for angiogenesis and tumor growth and formed a total of five clusters in the atlas (Fig. 6a). Four clusters emerged based on the function of these endothelial cells in supporting vasculature: endothelial vein, arterial, capillary, and lymphatic cells segregated based on expression of different marker genes (Fig 5a,b,c). A further cluster of immature endothelial cells (*Endo Imm*), defined by expression of *PLVAP, VWA1*, and *CA4*, was identified and has been implicated in poor tumor prognosis [38].

Other stromal subtypes captured in the atlas include vascular smooth muscle cells (*VSMC*) defined by expression of *RERGL*, and *MYH11*, extracellular matrix related pericytes (*ECM PCs*) defined by expression of collagen genes *COL4A1*, and *COL4A2*, as well as a set of proliferating stromal cells (*Prolif. Stromal)* characterized by high expression of proliferative markers including *TOP2A*, *MKI67*.

Taxonomic characterization of immune and stromal subtypes

We utilized K2Taxonomer to organize the clusters in the immune and stromal compartments into hierarchical taxonomies. Annotating groups of clusters, or clades, mitigates the uncertainty in annotation due to over-clustering. Taxonomic characterization also captures groups of cells sharing similar functions and cell states rather than just cell types.

In the immune compartment, cells largely segregated by lymphoid and myeloid lineages. The exceptions being a population of *pDCs*, which clustered with plasma cells in a clade due to their shared expression of *MZB1* [39], and Mast cells, which clustered within the lymphoid clade due to the lack of expression of macrophage and dendritic markers (*CD68*, *CD1C*). These exceptions suggest that immune cells in the TME may share similar transcriptional states despite having different lineages (Fig. 4b).

In the stromal compartment, cells partitioned by endothelial and non-endothelial at the first level, and within the non-endothelial clade, further separated between CAFs and mural cells,

and lastly between smooth muscle cells, pericytes, and myofibroblasts, indicating strong transcriptome-based partitioning of these stromal subtypes (Fig. 5b).

Cell type diversity of tumors changes across phenotypes

Using these improved annotations within the atlas, we used an entropy-based cell type diversity score (CTDS) [40] to assess how the overall diversity of the TME changes across patient phenotypes (Fig. 6a). The CTDS score yields the highest value when all cell types (or states) have equal representation in a sample, and the lowest value when a single cell type (or state) is represented in a sample.

Across clinical subtypes, the CTDS of observed epithelial cell states and stromal cell types observed was lowest in TNBC compared to ER+ and HER2+, whereas the average CTDS of immune cell types was highest in TNBC. Across age groups, we observed a consistent decrease in CTDS across all three compartments in older tumors compared to younger tumors. This expands upon previous studies that identified decreased immune cell type diversity in old subjects compared to young subjects, but only within PBMCs [40]. As tumor grade increased, we also observed a consistent decrease in cell type diversity within the epithelial and stromal compartment. The cell type diversity scores provide a global summary of changes in tumor heterogeneity that can complement the more granular differential abundance analysis of individual cell types within the tumor.

Improved estimates of differential immune cell type abundance across phenotypes

Using these improved annotations within the atlas, we used *sccomp* [41] to estimate differential immune cell type abundance across phenotypes such as tumor grade and subtype (Methods).

HER2+ tumors are typically considered to be 'hot' tumors with increased immune infiltration compared to other subtypes of tumors [42], but the details of their cell type composition vis-à-vis other tumor subtypes is unclear. In our analysis, we observed that one specific subset of T cells, *CD4 Tregs*, increased in abundance in HER2+ tumors relative to other tumor types, whereas one subset of macrophages, *Mac Col.*, decreased in relative abundance (Fig. 6b).

The immune microenvironment of ER+ tumors have been characterized as macrophage-driven, but the exact subtypes of macrophages driving this microenvironment remain unknown [43]. In our analysis, we observed that one subset of macrophages, *Mac Col.*, was enriched in ER+ tumors compared to other tumors (Fig. 6b).

TNBC tumors are known to have a heterogeneous immune microenvironment with tumors exhibiting both increased tumor infiltrating lymphocytes (TILS) [44], and increased tumor associated macrophages [45]. However, the exact nature of which immune cell types are enriched has not yet been characterized in studies with adequate statistical power. In our analysis we found that *Mac Lipo.* were enriched in TNBC tumors, as well as a subpopulation of *CLEC10A* conventional dendritic cells (*cDC2).* Previous studies have found that pDCs are expanded [46] and that mast cells are be depleted in TNBC tumors [47]. However, although these specific populations were also found to be expanded and depleted, respectively, in the atlas, their changes were not statistically significant (fdr > 0.05) (Fig. 6b).

Comparison of the atlas-based estimates of differential cell type abundances across tumor grades with the same estimates obtained on individual datasets further highlighted the utility of the integrated atlas to uncover unique associations (Fig. 6c). We found that significant

295 estimates of differential cell type abundance in the atlas were not significant or in discordant
296 directions when tested in individual datasets. For instance, *CD4 Tem* cells were observed to
297 increase with grade in two studies (Wang 2024 and Wu Natgen 2021) but after including all
298 the datasets in the atlas, they did not reach atlas-wide significance. Similarly, *Mast* cells
299 yielded no significant changes in two of the datasets tested (Pal 2021 and Wang 2024),
300 although when all datasets were combined in the atlas it was the cell type most significantly
301 decreasing with grade. Only three datasets were included in this comparison since datasets
302 need to have both high grade (grade 3) and low-grade tumors (grade 1 & 2) to be included in
303 this differential abundance analysis, which further highlights the need for integration so that
304 diverse patient and clinical metadata can be pooled in mega-analysis-based approaches.
305

306 ## Multi-resolution cell type associations with patient survival

307 To assess the clinical relevance of the subpopulations identified in the atlas, we performed
308 survival analyses by projecting bulk RNA expression data from both TCGA and METABRIC onto
309 the gene signatures that defined each subgroup within our taxonomic analyses (Fig. 7). To
310 correct for the confounding effects of patient age, proliferation, and inflammation with
311 respect to patient survival [29,48], the Cox proportional hazard model also included these factors
312 as covariates (Methods).
313
314 Two cell populations were significantly associated with survival in both TCGA and METABRIC
315 and both had a positive survival association (hazard ratio less than 1). These include a
316 subpopulation of epithelial cells (Cluster 5) which is characterized by low stemness (more
317 differentiated) and low grade (Fig 3a,c), and a cluster of *CD8 Tem* immune cells (Cluster 1).
318 Both CD8 effector memory T cell activity and cytotoxicity as well as low grade phenotype
319 within tumors have been previously associated with favorable prognosis in BC [29,49,50]. Though
320 no single cell type/state was associated with decreased survival in both datasets separately,
321 when combining the results by fisher's method, increased proliferative stromal cell (*Strom*
322 *Prolif*.) activity was collectively associated with decreased survival.

323 # *Discussion*

324 In this study we integrated scRNAseq data from 138 primary BC tumors collected across eight
325 studies to create the largest transcriptomic atlas of human BC to date. The large number of
326 patients in our integrated atlas, along with the rigorous annotation of both discrete cell types
327 and continuous cell states, will provide a valuable resource for researchers seeking to explore
328 associations of gene expression and or cell type composition with clinical and molecular
329 phenotypes with increased statistical power.
330
331 Our characterization of the cancer epithelial compartment of the atlas revealed substantial
332 heterogeneity between cancer cells along the axes of potency/stemness (differentiation
333 continuum), EMP (epithelial-mesenchymal continuum), expression of hallmark and HBCA
334 pathways, as well as clinical phenotypes. By leveraging K2Taxonomer and random forest
335 models, we performed a multi-resolution characterization of the cancer epithelial
336 compartment and identified the most discriminative factors differentiating epithelial clusters
337 at different levels of the taxonomy of BC epithelial cells. At the first level, we found that BC
338 tumor cells primarily segregated due to EMP, stemness, and basal phenotypes. At the second
339 level, tumor cells primarily segregated by age, suggesting that aging processes can be a major
340 driver of tumor heterogeneity [51]. At the third level, tumor cells separate through more granular
341 hallmark pathways, tumor subtype and grade. A multi-resolution characterization of cancer
342 cells has several advantages over typical unsupervised clustering approaches including
343 mitigating the risks of over-clustering and thus over-annotation, as well as being able to
344 identify the major factors driving heterogeneity in a dataset.

For the immune and stromal compartments, our analysis reconciled cell type information to established pan-cancer cell types previously characterized, and identified cell states unique to our BC atlas: a collagen expressing Macrophage subtype (*Mac Col.*) and exhausted CD4 cells (*CD4 Ex*), a T cell state associated with the progressive loss of cytokine production and effector function [52].

Using these annotations of immune cell type and state, we performed a cell type diversity and differential abundance analysis to capture global and more granular changes in cell type composition within the TME with respect to clinical phenotypes such as tumor subtype (ER+, HER2+, TNBC). Through the cell type diversity analysis, we uncovered associations between increasing tumor grade and decreasing global diversity within the TME, as well as age-associated changes across epithelial, stromal, and immune cells. Through the differential abundance analysis, we resolved differences in immune cell type composition unique to each subtype that provide insight into effective cancer therapies. The expansion of *Mac Lipo* in TNBC is of interest and may help explain recent findings suggesting that TNBC is uniquely susceptible to treatment with lipid-acting drugs [53]. The expansion of *CD4 Tregs* in HER2+ tumors, may explain the effectiveness of targeted therapies such as Traztuzumab that are known to modulate *Treg* activity [54], and highlights the need to identify additional therapies targeting *Treg* activity given that *CD4 Tregs* are known to promote an immunosuppressive TME that can lead to tumor escape [55]. The enrichment of conventional dendritic cells *cDC* and *Mac Col.* in TNBC and ER+, respectively, also represent promising targets for future therapies given their known role in antigen presentation to activate anti-tumor T cells and in remodeling the extracellular matrix, respectively [56,57]. Collectively, these subtype specific differences in the immune TME may help explain the effectiveness of existing cancer therapies and prioritize future targets. Further, by repeating this analysis in subsets of the atlas limited to the original datasets, we found that estimates of differential cell type abundance vary considerably between datasets, highlighting the need to pool data to arrive at more robust estimates and to increase the statistical significance of associations found between cell type composition and clinical phenotypes.

Finally, our atlas-wide survival analysis of cell type subpopulations based on bulk data from both TCGA and METABRIC (Supp Table 4) revealed both known associations, such as decreased mortality risk associated with increased CD8 memory T cell activity and low-grade cancer epithelial cells, as well as novel associations, such as increased mortality risk associated with increased proliferative stromal cells (*Strom Prolif.*), which could be prognostic in BC.

One limitation of this atlas is the absence of adipocytes, despite their known importance in cancer progression and aggressiveness [58], due to the technical limitations of scRNAseq. Other technologies such as single-nucleus RNA sequencing, and spatial transcriptomics are needed to characterize the heterogeneity in adipocytes across patients. Another limitation is that the atlas represents a static snapshot of the transcriptome and does not capture dynamic changes in response to treatments like radiation or chemotherapy, which could significantly alter the cellular composition and gene expression profiles. Future studies incorporating temporal analyses of cellular responses to various therapies could enhance the atlas' utility in guiding personalized treatment strategies and understanding mechanisms of treatment resistance.

In summary, this integrated scRNAseq BC atlas, the largest of its kind, fills a crucial need in our understanding of tumor heterogeneity by providing a ‘reference’ landscape of cell populations which not only enables statistically powered analyses of cell type diversity, composition, and survival, but also provides a framework for the construction of further atlases to interrogate tumor heterogeneity.

Methods

Data Acquisition

To create an unbiased scRNAseq atlas of human BC, we integrated publicly available datasets that contained untreated samples (samples from patients who had not undergone chemotherapy or other treatment before sequencing) and samples that were not sorted prior to sequencing (not biased towards a particular cell type). Given these criteria, we identified eight datasets to include in this atlas, totaling 138 patients and 621,200 cells.

Dataset	# Patients	# Cells	System	PMID	Data Link
Pal et al. 2021	33	224,823	10x 3'	33950524	GSE161529
Bassez et al. 2021	31	78,549	10x 5'	33958794	Lambrechts lab
Wu et al. 2021	26	99,876	10x 3' v2	34493872	GSE176078
Wang et al. 2024	14	48,553	10x 3' v2	38382468	GSE248288
Qian et al. 2020	14	40,665	10x 3' v2 & 10x 5' v2	32561858	Lambrechts lab
Tietscher et al. 2023	12	97,301	10x 3' v3	36609566	E-MTAB-10607
Liu et al. 2023	4	27,490	10x 3' v3	36594618	GSE225600
Gao et al. 2021	4	3,943	10x 3' v2 & 10x 5' v2	33462507	GSE148673
Total	**138**	**621,200**			

Table 1: Summary of Datasets used in Atlas

Data Preprocessing

Each scRNAseq dataset was first pre-processed using Seurat [59] to remove low-quality cells, doublets, and normalize data before integration. We adopted current scRNAseq pre-processing best-practices by using adaptive thresholding based on median absolute deviation, instead of manual cutoffs, to filter out outlier cells based on three criteria: mitochondrial genes expression, number of unique genes detected per cell, and total number of genes detected per cell [60,61]. For studies that only provided pre-filtered data, we retained all cells for downstream analysis. Following filtering, doublet scores were obtained using scDblFinder [62] and expression profiles were normalized by total expression and log-transformed using Seurat's *LogNormalize* function which has been demonstrated to work well in prior benchmarking [63].

Integration of Single Cell Data

Integration of filtered scRNAseq data was performed using various methods: Seurat's V5 reciprocal principal component analysis (RPCA) [59], fastMNN [64], Harmony [65], scVI [66], and scANVI [67]. To facilitate fair comparison between the integration methods, the same number of variable features (5000), and PC dimensions (200) were used for integration when possible. For scVI and scANVI, integration is performed at the level of raw counts instead of embeddings, so only the variable feature selection process was included. To avoid biasing the integration towards individual sources of annotations e.g. author annotations or SingleR/CellTypist annotations, only the batch correction metrics: silhouette score, k-nearest neighbor batch effect test (kBET), and integration local inverse Simpson's index (iLISI), were used to assess integration performance. The best performing integration according to these metrics – Seurat V5's RPCA, was chosen for downstream analysis (Fig 2a).

Inference of PAM50 Subtype

To infer molecular subtypes of each sample using the PAM50 method, we first calculated a 'pseudo-bulk' profile for each tumor using Seurat's *AggregateExpression* function, and then

applied *molecular.subtyping* from the *genefu* R package to each pseudo-bulk profile with default parameters [68].

Discrete annotation of cell types

Annotation of cell types was performed using a combination of reference based annotation methods: singleR [30], CellTypist [31,69], unsupervised recursive partitioning: K2Taxonomer [29], and unsupervised clustering followed by differential expression analysis: MAST [32].

Reference-based annotation of cell type

Both singleR and CellTypist require a labelled scRNAseq reference dataset to compare query cells with. Since all of the samples in this study originate from breast tissue, we leveraged labeled scRNAseq data from the healthy breast cell atlas (HBCA) as reference [10]. For singleR, the wilcox method *de.method = "Wilcox"* was used as this is more appropriate than the default methods when applying singleR to single cell data. For CellTypist, we used a pre-trained breast tissue model that used labeled data from HBCA [69], and used majority voting to determine the final cell type label *majority_voting = True, mode = 'best match'*.

Unsupervised clustering-based annotation

Both K2Taxonomer and MAST-based annotation rely on unsupervised clustering which was performed using the Louvain algorithm for three subsets of the atlas separately: epithelial, immune, and stromal, based on expression of canonical markers (Epithelial: *EPCAM, KRT8, KRT 18*; Immune*: PTPRC, CD3D, CD3E, CD68*; Stromal: *COL1A1, COL1A2, ENG*). Performing clustering and annotation within each compartment separately enables the detailed characterization of heterogeneity within each compartment.

To identify differentially expressed genes (DEGs) between clusters, we used Seurat's *FindAllMarkers* with the parameters *test.use = 'MAST'*, and *latent.vars = 'batch'* to account for the negative-binomial distribution of single cell data and to control for dataset-specific effects respectively.

Whilst methods like MAST can quantify differences at the cluster level, the number of clusters, and the resulting DEGs obtained from downstream analysis, relies heavily on arbitrary values of the 'resolution' parameter in typical unsupervised clustering algorithms. To mitigate these limitations, we leveraged K2Taxonomer to learn hierarchical relationships between the clusters identified in each compartment, enabling the annotation of clades of clusters instead of just individual clusters. To accomplish this, K2Taxonomer was applied to the integrated embeddings obtained from RPCA, with the following parameters (*featMetric="F", nBoots=400, clustFunc=cKmeansDownsampleSqrt*) which are recommended for large scRNAseq datasets [29]. To estimate the differentially expressed genes (DEGs) between nodes in the dendrogram, we used the normalized gene expression matrix and K2Taxonomer's built in function *runDGEmods* with batch variable as a covariate to control for dataset-specific effects.

Random Forest-based annotation of discriminative factors

The *randomForest* package was used to train random forests to classify cluster membership, or meta-cluster membership (as determined by K2 Taxonomer), of single cell profiles based on expression of continuous scores related to cell stemness, EMP, HBCA cell type, malignancy, and clinical metadata. The model was run with the parameter *importance = TRUE* to extract the most important features (as determined by gini-based importances), that differentiated epithelial clusters from each other.

Continuous annotation of cell states

Classifying discrete cell types is just one facet of heterogeneity, and there are many transient functional programs or cell states that require a more continuous scoring [70]. To characterize heterogeneity of functional states within the cancer epithelial compartment of our BC atlas we scored each cell in terms of its malignancy with inferCNV [27], stemness with Cytotrace2 [25], Epithelial-Mesenchymal plasticity [26], expression of hallmark pathways [28,71], as well as expression of epithelial subtypes identified in HBCA [10].

Inference of copy number variations

InferCNV was used to estimate copy number alterations for tumor epithelial cells from each dataset independently with the following parameters: *cutoff = 0.1*, *cluster_by_groups = TRUE*, *denoise = TRUE* and *HMM = FALSE* that are recommended for 10X scRNAseq data. Immune and stromal cells from each dataset were used as normal references, and from these normal reference sets, 100 immune and stromal cells were sampled to act as negative controls to validate inferCNV output.

For each cell, inferCNV estimates a score for each gene that is above one if there is inferred copy number gain, and below one if there is inferred copy number loss. We summarized these scores to estimate a malignancy score per cell that represents the mean absolute CNV score.

$$Malignancy\ Score = \frac{\sum |CNV\ score|}{\#Genes}$$

To classify each cell as malignant or non-malignant, for each dataset we found the 90% interval of malignancy scores of the negative control cells (non-epithelial cells) and labeled all epithelial cells outside of this interval as malignant (Supp Fig. 6).

Scoring of gene set activity

To characterize the heterogeneity of functional states present in the atlas, we leveraged publicly available transcriptional signatures (Supp Table 4) and used a rank-based method (AUCell) [72], with default parameters, to score enrichment of signatures in each cell. For the immune compartment, we scored cells using signatures from pan-cancer studies of myeloid and lymphoid cell states [33,35], as well as signatures of immune cell types from HBCA [10]. For the stromal compartment, we scored cells using signatures from a pan-cancer study of stromal cell heterogeneity [38]. For the epithelial compartment, we scored cells using canonical hallmark signatures [28], as well as signatures of epithelial cell types from HBCA [10].

Differential Diversity and Abundance Analysis

Cell Type Diversity Analysis

We used an entropy-based cell type diversity metric (CTDS) [40] to assess how the overall diversity in a patient's TME changes across subtype, age, and tumor grade. The CTDS metric accounts for the number of cells per sample and the compositional nature of proportional data which enables comparison across samples.

Differential Abundance Analysis

To test differences in cell type proportions across different phenotype groups e.g. tumor grade and subtype, we used the R package *sccomp* with *bimodal_mean_variability_association = TRUE* which is recommended for scRNAseq data [41]. To isolate the effects of tumor grade on TME composition, we controlled for tumor subtype, age, and batch with the following formula:

$$celltype_{count} \sim grade + pam50 + age + (1|batch)$$

Similarly, to isolate the effects of tumor subtype on TME composition, we controlled for grade, age, and batch.

$$celltype_{count} \sim (LumA/LumB/Her2/Normal_like) + grade + age + (1|batch)$$

Multi-resolution survival analysis of cell type populations

To identify the clinical relevance of cell type annotations identified in the atlas, we extracted differentially expressed genes defining each subpopulation found in our taxonomic analysis of each compartment (K2Taxonomer) [29], and used the R package *brcasurv* [73] to model the association between the expression of subpopulation specific genes and patient survival in both TCGA [3] and METABRIC [74].

To address possible confounders in the survival analysis, we included patients age, as well as patient-level gene set projection scores of inflammation and proliferation that have previously been associated with poor prognosis and demonstrated to be necessary for correction in survival modelling [29,48,75]. The patient-level gene set scores were obtained by using the R package *GSVA* [76] to project inflammation [75], proliferation [48], as well as the cell type specific gene sets onto transcriptional profiles from TCGA and METABRIC. The Cox proportional hazards model underlying the survival analysis controlled for these confounders with the following formula:

$$Surv(patient) \sim celltype_{gsva} + age + inflam_{gsva} + prolif_{gsva}$$

To control for multiple testing, we corrected p-values in each cox model using the FDR method [77] in the *p.adjust* R package, and to reconcile p-values between analyses performed in TCGA and METABRIC, we used the Fisher's method for combining p-values [78].

Data Availability

All code is available at: https://github.com/montilab/brca_atlas and figshare https://doi.org/10.6084/m9.figshare.28685012.v1.

Author contributions

A.C. performed all analyses and wrote the manuscript.
L.K., and S.M. provided computational guidance and feedback.
C.S.E., L.K., and G.V.D, provided biological guidance.
S.M. oversaw the project.
The manuscript was edited by all authors.

Acknowledgments

We thank Gat Rauner, and Yuhan Qiu for feedback regarding the construction and annotation of the atlas. We also thank Corinn Small for providing thorough feedback on making the data accessible on cellxgene. This work was supported by grants from the National Institute of Health (NIH): U01CA243004 (G.V.D. and S.M.), the National Institute of General Medical Sciences of the NIH under award number T32GM100842, and by a gift from Find The Cause Breast Cancer Foundation [79]. The content is solely the responsibility of the authors and does not necessarily represent the official views of the NIH.

Competing interests

There are no conflicts to be declared.

Figure Legends

Figure 1. Construction and composition of the integrated breast cancer atlas. A) Overview of the construction of the integrated atlas and downstream analysis. B) Distribution of patients

575 and number of cells per patient sequenced across each of the eight datasets. C) Distribution
576 of tumor subtype and grade information. D) Distribution of ages for all patient donors.
577
578 Figure 2. Compartment specific analysis of atlas. A) Batch correction metrics for each
579 integration method. B) UMAP of embeddings from chosen integration method (RPCA) and the
580 separation by broad cell type. C) Expression of canonical markers for each of the broad cell
581 types separated from the atlas. D) Distribution of cells from each dataset in each of the three
582 broad compartments. E) Comparison of broad cell type label between author annotations and
583 atlas-based annotations. F) Expression of canonical markers for the relabeled cells if
584 categorized by the atlas labels. G) Expression of canonical markers for the relabeled cells if
585 categorized by their original labels.
586
587 Figure 3. Multi-resolution characterization of Cancer Epithelial Compartment. A) Heatmap of
588 patient metadata, malignancy data (InferCNV), annotation data (HBCA), cell potency data
589 (Cytotrace), plasticity data (EMP), and expression of hallmark pathways (Hallmark). B)
590 Dendrogram of epithelial clusters learned from K2 Taxonomer. C) Top 5 important features,
591 as determined by gini-based importance, from random forest models trained to differentiate
592 different clades within each level of the dendrogram. Red cells indicate that scores related to
593 that feature were higher than the mean in that subset of the dataset.
594
595 Figure 4. Diversity of immune cell types in the TME. A) Sankey diagram of all immune subtypes
596 characterized in the atlas. B) Dendrogram of immune annotations learned from K2 Taxonomer.
597 C) Dot plot of markers for the lymphoid subtypes identified in the atlas. D) Dot plot of markers
598 for the myeloid subtypes identified in the atlas.
599
600 Figure 5. Diversity of stromal cell types in the TME. A) Sankey diagram of all stromal subtypes
601 characterized in the atlas. B) Dendrogram of stromal annotations learned from K2 Taxonomer.
602 C) Dot plot of markers for the stromal subtypes identified in the atlas.
603
604 Figure 6. Differential cell type diversity and abundance analysis. A) Cell Type Diversity Score
605 (CTDS) across tumor subtype, patient age, and tumor grade. B) Differential cell type estimates
606 within the immune compartment between HER2+, ER+ and TNBC tumors. B) Differential cell
607 type estimates within the immune compartment between high and low grade tumors.
608
609 Figure 7. Survival associations of subpopulations found within taxonomic analysis of epithelial,
610 stromal, and immune compartments with respect to TCGA and METABRIC. Green branches
611 indicate a clade that confers a survival advantage (hazard ratio < 1), and red branches indicate
612 a survival disadvantage (hazard ratio > 1) in the respective dataset.
613
614 Supplementary Figure 1. UMAP of unintegrated data colored by dataset, subtype, grade, cell
615 typist, singleR, and author annotation.
616
617 Supplementary Figure 2. UMAP of RPCA integrated data colored by clustering, and broad cell
618 type annotations from singleR, CellTypist, and author provided metadata.
619
620 Supplementary Figure 3. Cancer Epithelial Compartment Diversity. A) UMAP of cancer
621 epithelial cells colored by clustering performed at 0.2 resolution. B) UMAP of cancer epithelial
622 cells colored by HBCA annotation from CellTypist. C) UMAP of cancer epithelial cells colored
623 by tumor subtype. D) UMAP of cancer epithelial cells colored by PAM 50 subtype. E)
624 Distribution of patients across each of the clusters. F) Entropy of donor proportions across
625 each of the clusters.
626

627 Supplementary Figure 4. UMAP of immune compartment colored by clustering, and cell type
628 annotations from singleR, CellTypist, and author provided metadata.
629
630 Supplementary Figure 5. UMAP of stromal compartment colored by clustering, and cell type
631 annotations from singleR, CellTypist, and author provided metadata.
632
633 Supplementary Figure 6. Distribution of inferCNV scores for each of the datasets included in
634 the atlas. Immune and stromal cells sampled from each donor are in yellow whereas epithelial
635 cells are in orange. The empirical 90% interval of malignancy scores for normal cells is
636 highlighted for each dataset and is the interval used to classify epithelial cells as malignant or
637 non-malignant.

638 ## References

639 1. Siegel, R. L., Giaquinto, A. N. & Jemal, A. Cancer statistics, 2024. *CA Cancer J. Clin.* **74**, 12–
640 49 (2024).

641 2. Perou, C. M. *et al.* Molecular portraits of human breast tumours. *Nature* **406**, 747–752
642 (2000).

643 3. Cancer Genome Atlas Network. Comprehensive molecular portraits of human breast
644 tumours. *Nature* **490**, 61–70 (2012).

645 4. Polyak, K. Breast cancer: origins and evolution. *J. Clin. Invest.* **117**, 3155–3163 (2007).

646 5. Lüönd, F., Tiede, S. & Christofori, G. Breast cancer as an example of tumour heterogeneity
647 and tumour cell plasticity during malignant progression. *Br. J. Cancer* **125**, 164–175
648 (2021).

649 6. Place, A. E., Jin Huh, S. & Polyak, K. The microenvironment in breast cancer progression:
650 biology and implications for treatment. *Breast Cancer Res.* **13**, 227 (2011).

651 7. Kolodziejczyk, A. A., Kim, J. K., Svensson, V., Marioni, J. C. & Teichmann, S. A. The
652 technology and biology of single-cell RNA sequencing. *Mol. Cell* **58**, 610–620 (2015).

653 8. Fleck, J. S., Camp, J. G. & Treutlein, B. What is a cell type? *Science* **381**, 733–734 (2023).

654 9. Reed, A. D. *et al.* A single-cell atlas enables mapping of homeostatic cellular shifts in the
655 adult human breast. *Nat. Genet.* **56**, 652–662 (2024).

656 10. Kumar, T. *et al.* A spatially resolved single-cell genomic atlas of the adult human breast.
657 *Nature* **620**, 181–191 (2023).

658 11. Pal, B. *et al.* A single-cell RNA expression atlas of normal, preneoplastic and tumorigenic
659 states in the human breast. *EMBO J.* **40**, e107333 (2021).

660 12. Wu, S. Z. *et al.* A single-cell and spatially resolved atlas of human breast cancers. *Nat.*
661 *Genet.* **53**, 1334–1347 (2021).

662 13. Tietscher, S. *et al.* A comprehensive single-cell map of T cell exhaustion-associated

663 immune environments in human breast cancer. *Nat. Commun.* **14**, 98 (2023).

664 14. Bassez, A. *et al.* A single-cell map of intratumoral changes during anti-PD1 treatment of
665 patients with breast cancer. *Nat. Med.* **27**, 820–832 (2021).

666 15. Wang, L. *et al.* PD-L1-expressing tumor-associated macrophages are immunostimulatory
667 and associate with good clinical outcome in human breast cancer. *Cell Rep. Med.* **5**,
668 101420 (2024).

669 16. Qian, J. *et al.* A pan-cancer blueprint of the heterogeneous tumor microenvironment
670 revealed by single-cell profiling. *Cell Res.* **30**, 745–762 (2020).

671 17. Liu, Y.-M. *et al.* Combined single-cell and spatial transcriptomics reveal the metabolic
672 evolvement of breast cancer during early dissemination. *Adv. Sci. (Weinh.)* **10**, e2205395
673 (2023).

674 18. Gao, R. *et al.* Delineating copy number and clonal substructure in human tumors from
675 single-cell transcriptomes. *Nat. Biotechnol.* **39**, 599–608 (2021).

676 19. Wu, S. Z. *et al.* Stromal cell diversity associated with immune evasion in human triple-
677 negative breast cancer. *EMBO J.* **39**, e104063 (2020).

678 20. Wu, S. Z. *et al.* Cryopreservation of human cancers conserves tumour heterogeneity for
679 single-cell multi-omics analysis. *Genome Med.* **13**, 81 (2021).

680 21. Xu, L. *et al.* A comprehensive single-cell breast tumor atlas defines epithelial and immune
681 heterogeneity and interactions predicting anti-PD-1 therapy response. *Cell Rep Med*
682 101511 (2024).

683 22. Johnston, K. G., Grieco, S. F., Nie, Q., Theis, F. J. & Xu, X. Small data methods in omics: the
684 power of one. *Nat. Methods* (2024) doi:10.1038/s41592-024-02390-8.

685 23. Luecken, M. D. *et al.* Benchmarking atlas-level data integration in single-cell genomics.
686 *Nat. Methods* **19**, 41–50 (2022).

687 24. Sun, X.-X. & Yu, Q. Intra-tumor heterogeneity of cancer cells and its implications for

688 cancer treatment. *Acta Pharmacol. Sin.* **36**, 1219–1227 (2015).

689 25. Gulati, G. S. *et al.* Single-cell transcriptional diversity is a hallmark of developmental
690 potential. *Science* **367**, 405–411 (2020).

691 26. Winkler, J. *et al.* Single-cell analysis of breast cancer metastasis reveals epithelial-
692 mesenchymal plasticity signatures associated with poor outcomes. *J. Clin. Invest.* **134**,
693 (2024).

694 27. Tickle, T., Tirosh, I., Georgescu, C., Brown, M. & Haas, B. inferCNV of the Trinity CTAT
695 Project. Preprint at https://github.com/broadinstitute/inferCNV (2019).

696 28. Liberzon, A. *et al.* The Molecular Signatures Database (MSigDB) hallmark gene set
697 collection. *Cell Syst* **1**, 417–425 (2015).

698 29. Reed, E. R. & Monti, S. Multi-resolution characterization of molecular taxonomies in bulk
699 and single-cell transcriptomics data. *Nucleic Acids Res.* **49**, e98 (2021).

700 30. Aran, D. *et al.* Reference-based analysis of lung single-cell sequencing reveals a
701 transitional profibrotic macrophage. *Nat. Immunol.* **20**, 163–172 (2019).

702 31. Domínguez Conde, C. *et al.* Cross-tissue immune cell analysis reveals tissue-specific
703 features in humans. *Science* **376**, eabl5197 (2022).

704 32. Finak, G. *et al.* MAST: a flexible statistical framework for assessing transcriptional changes
705 and characterizing heterogeneity in single-cell RNA sequencing data. *Genome Biol.* **16**,
706 278 (2015).

707 33. Guimarães, G. R. *et al.* Single-cell resolution characterization of myeloid-derived cell
708 states with implication in cancer outcome. *Nat. Commun.* **15**, 5694 (2024).

709 34. Strack, E. *et al.* Identification of tumor-associated macrophage subsets that are
710 associated with breast cancer prognosis. *Clin. Transl. Med.* **10**, e239 (2020).

711 35. Chu, Y. *et al.* Pan-cancer T cell atlas links a cellular stress response state to
712 immunotherapy resistance. *Nat Med* **29**, 1550–1562 (2023).

713 36. Zheng, L. *et al.* Pan-cancer single-cell landscape of tumor-infiltrating T cells. *Science* **374**,
714 abe6474 (2021).

715 37. Kiselev, V. Y., Andrews, T. S. & Hemberg, M. Challenges in unsupervised clustering of
716 single-cell RNA-seq data. *Nat. Rev. Genet.* **20**, 273–282 (2019).

717 38. Du, Y. *et al.* Integration of Pan-Cancer Single-Cell and Spatial Transcriptomics Reveals
718 Stromal Cell Features and Therapeutic Targets in Tumor Microenvironment. *Cancer Res.*
719 **84**, 192–210 (2024).

720 39. Kapoor, T., Corrado, M., Pearce, E. L., Pearce, E. J. & Grosschedl, R. MZB1 enables efficient
721 interferon α secretion in stimulated plasmacytoid dendritic cells. *Sci. Rep.* **10**, 21626
722 (2020).

723 40. Karagiannis, T. T., Monti, S. & Sebastiani, P. Cell Type Diversity Statistic: An Entropy-Based
724 Metric to Compare Overall Cell Type Composition Across Samples. *Front. Genet.* **13**,
725 855076 (2022).

726 41. Mangiola, S. *et al.* sccomp: Robust differential composition and variability analysis for
727 single-cell data. *Proc. Natl. Acad. Sci. U. S. A.* **120**, e2203828120 (2023).

728 42. Perrone, M., Talarico, G., Chiodoni, C. & Sangaletti, S. Impact of immune cell
729 heterogeneity on HER2+ breast cancer prognosis and response to therapy. *Cancers*
730 *(Basel)* **13**, 6352 (2021).

731 43. Onkar, S. *et al.* Immune landscape in invasive ductal and lobular breast cancer reveals a
732 divergent macrophage-driven microenvironment. *Nat. Cancer* **4**, 516–534 (2023).

733 44. Fan, Y. & He, S. The characteristics of tumor microenvironment in triple negative breast
734 cancer. *Cancer Manag. Res.* **14**, 1–17 (2022).

735 45. Yuan, Z.-Y., Luo, R.-Z., Peng, R.-J., Wang, S.-S. & Xue, C. High infiltration of tumor-
736 associated macrophages in triple-negative breast cancer is associated with a higher risk
737 of distant metastasis. *Onco. Targets. Ther.* **7**, 1475–1480 (2014).

738 46. Oshi, M. *et al.* Plasmacytoid dendritic cell (pDC) infiltration correlate with tumor
739 infiltrating lymphocytes, cancer immunity, and better survival in triple negative breast
740 cancer (TNBC) more strongly than conventional dendritic cell (cDC). *Cancers (Basel)* **12**,
741 3342 (2020).

742 47. Majorini, M. T., Colombo, M. P. & Lecis, D. Few, but efficient: The role of mast cells in
743 breast cancer and other solid tumors. *Cancer Res.* **82**, 1439–1447 (2022).

744 48. Venet, D., Dumont, J. E. & Detours, V. Most random gene expression signatures are
745 significantly associated with breast cancer outcome. *PLoS Comput. Biol.* **7**, e1002240
746 (2011).

747 49. Jin, Y. *et al.* Prognostic impact of memory CD8(+) T cells on immunotherapy in human
748 cancers: A systematic review and meta-analysis. *Front. Oncol.* **11**, 698076 (2021).

749 50. Henson, D. E., Ries, L., Freedman, L. S. & Carriaga, M. Relationship among outcome, stage
750 of disease, and histologic grade for 22,616 cases of breast cancer. The basis for a
751 prognostic index. *Cancer* **68**, 2142–2149 (1991).

752 51. Chatsirisupachai, K., Lagger, C. & de Magalhães, J. P. Age-associated differences in the
753 cancer molecular landscape. *Trends Cancer* **8**, 962–971 (2022).

754 52. Miggelbrink, A. M. *et al.* CD4 T-cell exhaustion: Does it exist and what are its roles in
755 cancer? *Clin. Cancer Res.* **27**, 5742–5752 (2021).

756 53. Scully, T., Kase, N., Gallagher, E. J. & LeRoith, D. Regulation of low-density lipoprotein
757 receptor expression in triple negative breast cancer by EGFR-MAPK signaling. *Sci. Rep.* **11**,
758 17927 (2021).

759 54. Horlock, C. *et al.* The effects of trastuzumab on the CD4+CD25+FoxP3+ and CD4+IL17A+
760 T-cell axis in patients with breast cancer. *Br. J. Cancer* **100**, 1061–1067 (2009).

761 55. Plitas, G. *et al.* Regulatory T cells exhibit distinct features in human breast cancer.
762 *Immunity* **45**, 1122–1134 (2016).

763 56. Sebastião, A. I. *et al.* Dendritic cells in triple-negative breast cancer: From
764 pathophysiology to therapeutic applications. *Cancer Treat. Rev.* **133**, 102884 (2025).
765 57. Deligne, C. & Midwood, K. S. Macrophages and extracellular matrix in breast cancer:
766 Partners in crime or protective allies? *Front. Oncol.* **11**, 620773 (2021).
767 58. Gao, Y. *et al.* Adipocytes promote breast tumorigenesis through TAZ-dependent secretion
768 of Resistin. *Proc. Natl. Acad. Sci. U. S. A.* **117**, 33295–33304 (2020).
769 59. Hao, Y. *et al.* Integrated analysis of multimodal single-cell data. *Cell* **184**, 3573-3587.e29
770 (2021).
771 60. Heumos, L. *et al.* Best practices for single-cell analysis across modalities. *Nat. Rev. Genet.*
772 **24**, 550–572 (2023).
773 61. Amezquita, R. A. *et al.* Orchestrating single-cell analysis with Bioconductor. *Nat. Methods*
774 **17**, 137–145 (2020).
775 62. Germain, P.-L., Lun, A., Garcia Meixide, C., Macnair, W. & Robinson, M. D. Doublet
776 identification in single-cell sequencing data using scDblFinder. *F1000Res.* **10**, 979 (2021).
777 63. Ahlmann-Eltze, C. & Huber, W. Comparison of transformations for single-cell RNA-seq
778 data. *Nat. Methods* **20**, 665–672 (2023).
779 64. Haghverdi, L., Lun, A. T. L., Morgan, M. D. & Marioni, J. C. Batch effects in single-cell RNA-
780 sequencing data are corrected by matching mutual nearest neighbors. *Nat. Biotechnol.*
781 **36**, 421–427 (2018).
782 65. Korsunsky, I. *et al.* Fast, sensitive and accurate integration of single-cell data with
783 Harmony. *Nat. Methods* **16**, 1289–1296 (2019).
784 66. Lopez, R., Regier, J., Cole, M. B., Jordan, M. I. & Yosef, N. Deep generative modeling for
785 single-cell transcriptomics. *Nat. Methods* **15**, 1053–1058 (2018).
786 67. Xu, C. *et al.* Probabilistic harmonization and annotation of single-cell transcriptomics data
787 with deep generative models. *Mol. Syst. Biol.* **17**, e9620 (2021).

788 68. Gendoo, D. M. A. *et al.* Genefu: an R/Bioconductor package for computation of gene
789 expression-based signatures in breast cancer. *Bioinformatics* **32**, 1097–1099 (2016).

790 69. Xu, C. *et al.* Automatic cell-type harmonization and integration across Human Cell Atlas
791 datasets. *Cell* **186**, 5876-5891.e20 (2023).

792 70. Dance, A. What is a cell type, really? The quest to categorize life's myriad forms. *Nature*
793 **633**, 754–756 (2024).

794 71. Subramanian, A. *et al.* Gene set enrichment analysis: a knowledge-based approach for
795 interpreting genome-wide expression profiles. *Proc. Natl. Acad. Sci. U. S. A.* **102**, 15545–
796 15550 (2005).

797 72. Aibar, S. *et al.* SCENIC: single-cell regulatory network inference and clustering. *Nat.*
798 *Methods* **14**, 1083–1086 (2017).

799 73. Chen, A. *Brcasurv*. (2025).

800 74. Curtis, C. *et al.* The genomic and transcriptomic architecture of 2,000 breast tumours
801 reveals novel subgroups. *Nature* **486**, 346–352 (2012).

802 75. Winslow, S., Leandersson, K., Edsjö, A. & Larsson, C. Prognostic stromal gene signatures
803 in breast cancer. *Breast Cancer Res.* **17**, 23 (2015).

804 76. Hänzelmann, S., Castelo, R. & Guinney, J. GSVA: gene set variation analysis for microarray
805 and RNA-seq data. *BMC Bioinformatics* **14**, 7 (2013).

806 77. Benjamini, Y. & Hochberg, Y. Controlling the false discovery rate: a practical and powerful
807 approach to multiple testing. *Journal of the royal statistical society series b-*
808 *methodological* **57**, 289–300 (1995).

809 78. Fisher, R. A. *Statistical Methods for Research Workers*. vol. no. V (Oliver and Boyd,
810 Edinburgh, 1938).

811 79. Find The Cause Breast Cancer Foundation. https://findthecausebcf.org/ (2016).

Figure 1

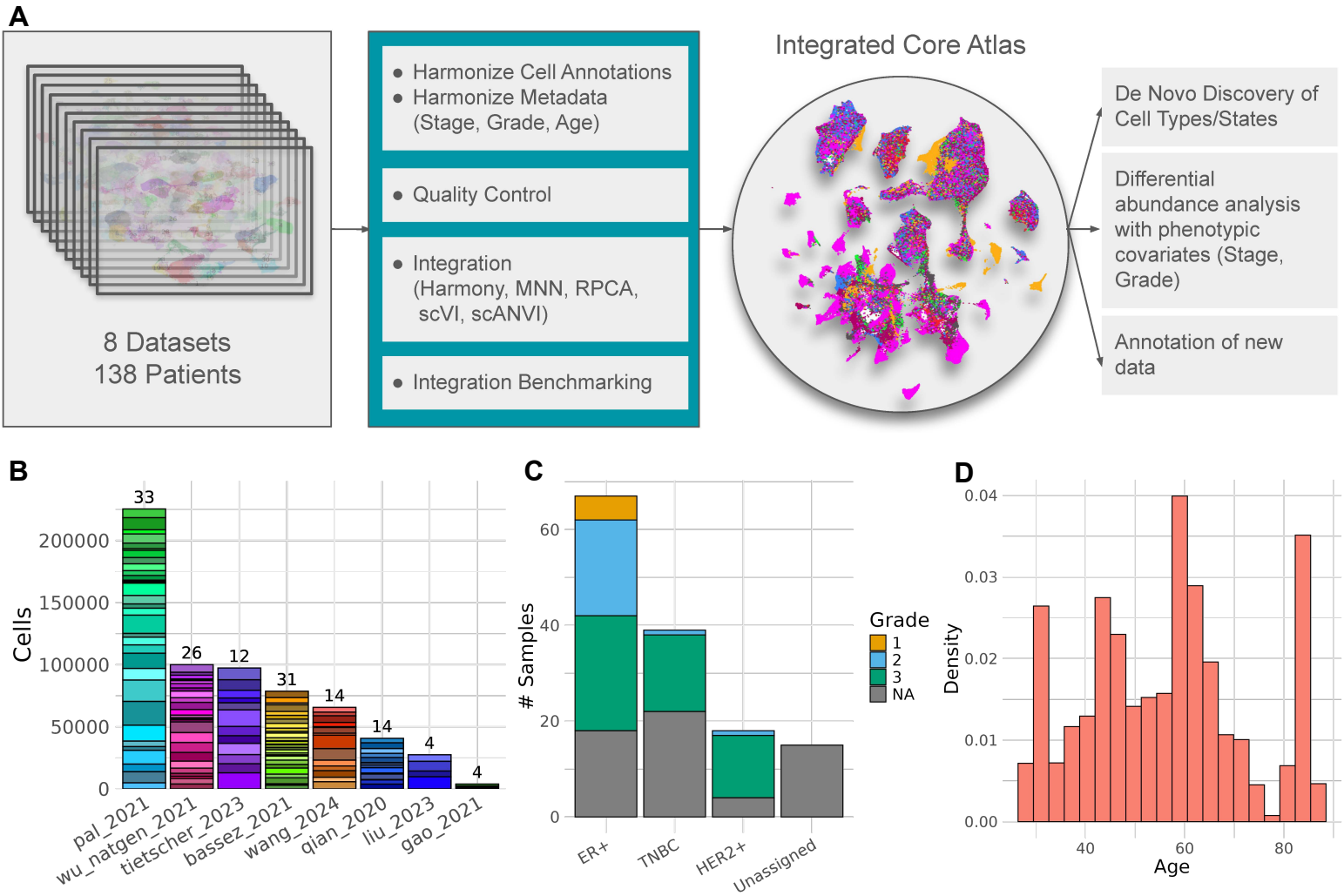
A
8 Datasets
138 Patients
Harmonize Cell Annotations
Harmonize Metadata (Stage, Grade, Age)
Quality Control
Integration (Harmony, MNN, RPCA, scVI, scANVI)
Integration Benchmarking
Integrated Core Atlas
De Novo Discovery of Cell Types/States
Differential abundance analysis with phenotypic covariates (Stage, Grade)
Annotation of new data
B
Cells
33
26
12
31
14
14
4
4
pal_2021
wu_natgen_2021
tietscher_2023
bassez_2021
wang_2024
qian_2020
liu_2023
gao_2021
C
Samples
ER+
TNBC
HER2+
Unassigned
Grade
1
2
3
NA
D
Density
Age

Figure 2

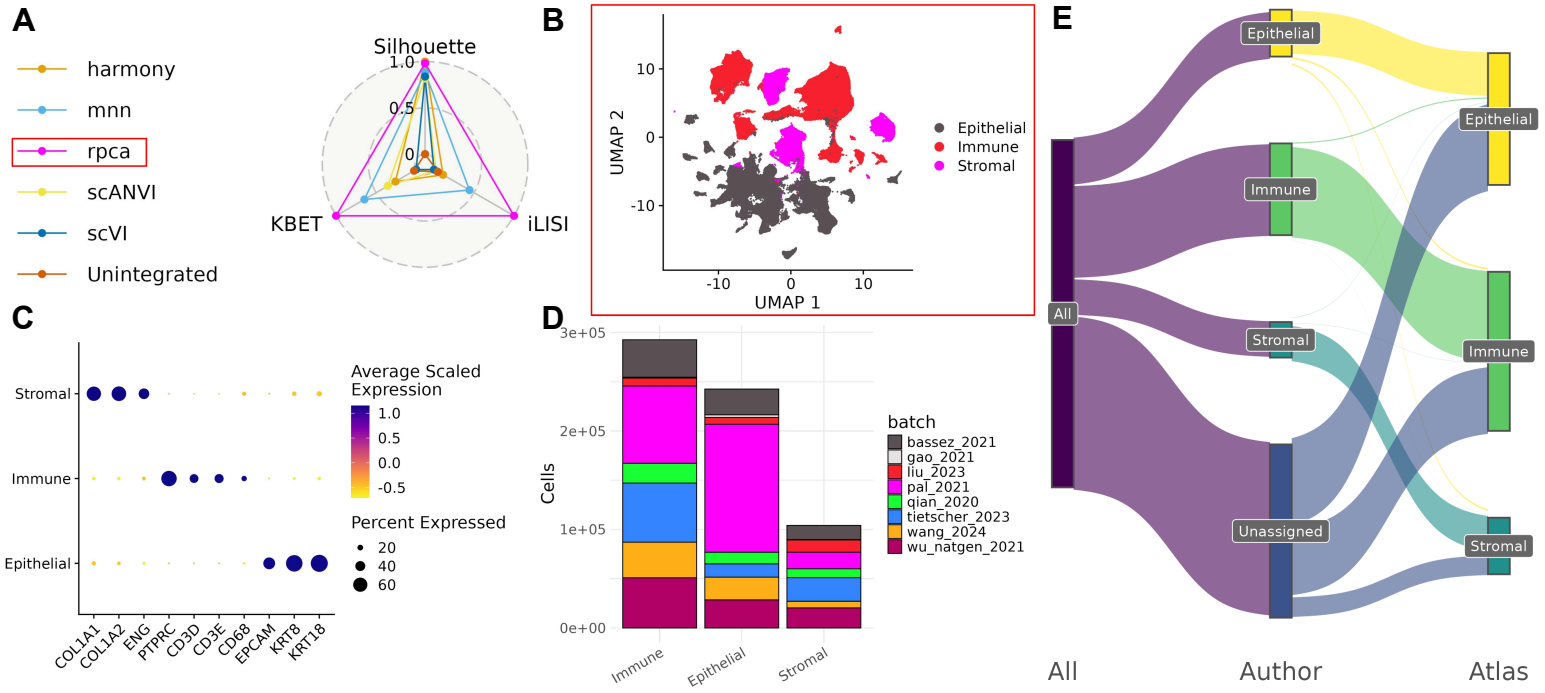
A
harmony
mnn
rpca
scANVI
scVI
Unintegrated
Silhouette
1.0
0.5
0
KBET
iLISI
B
UMAP 2
UMAP 1
10
0
-10
Epithelial
Immune
Stromal
C
Stromal
Immune
Epithelial
COL1A1
COL1A2
ENG
PTPRC
CD3D
CD3E
CD68
EPCAM
KRT8
KRT18
Average Scaled Expression
1.0
0.5
0.0
-0.5
Percent Expressed
20
40
60
D
Cells
3e+05
2e+05
1e+05
0e+00
Immune
Epithelial
Stromal
batch
bassez_2021
gao_2021
liu_2023
pal_2021
qian_2020
tietscher_2023
wang_2024
wu_natgen_2021
E
All
Epithelial
Immune
Stromal
Unassigned
Epithelial
Immune
Stromal
All
Author
Atlas

Figure 3

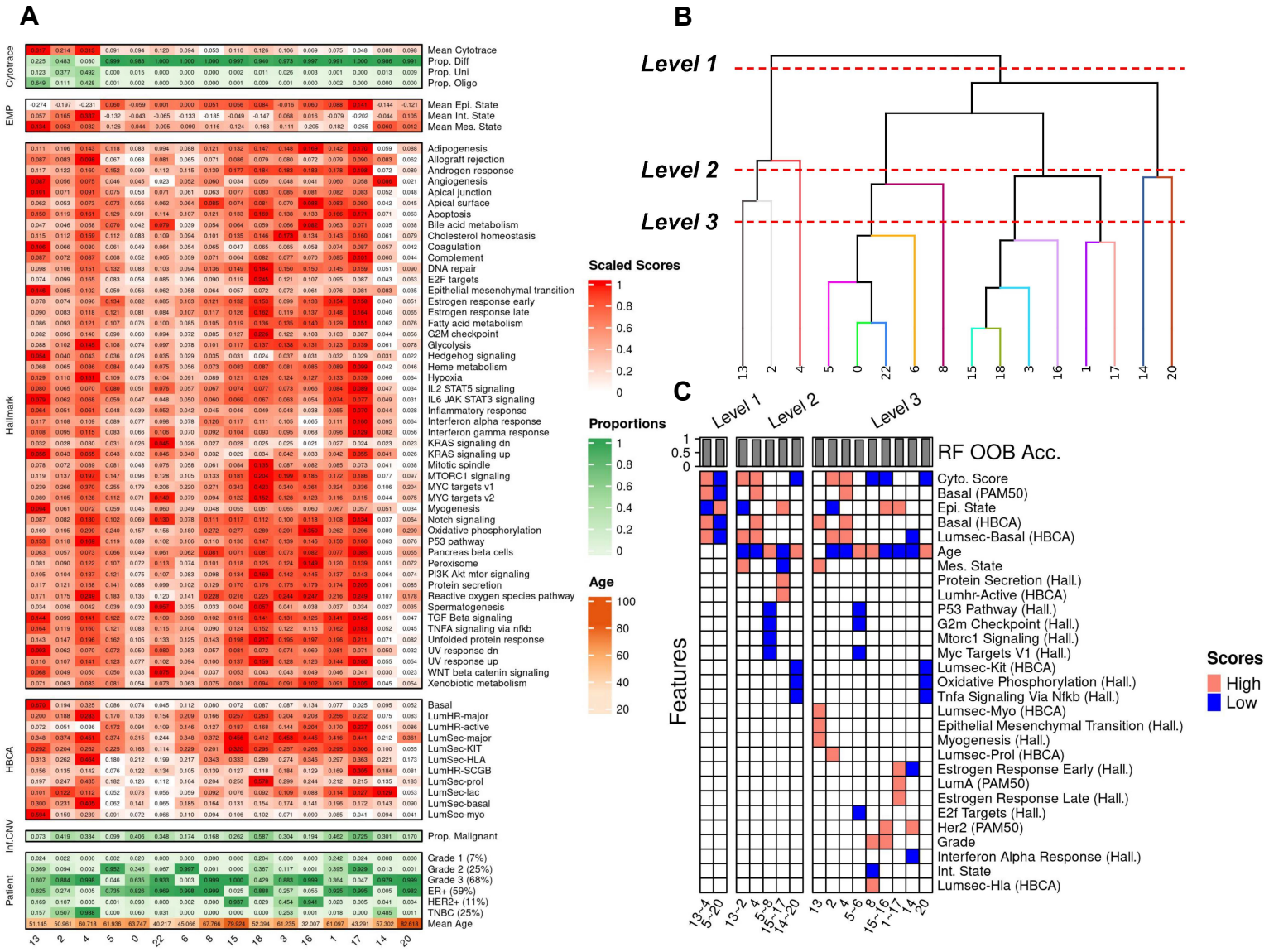
A
B
C
Cytotrace
Mean Cytotrace
Prop. Diff
Prop. Uni
Prop. Oligo
EMP
Mean Epi. State
Mean Int. State
Mean Mes. State
Hallmark
Adipogenesis
Allograft rejection
Androgen response
Angiogenesis
Apical junction
Apical surface
Apoptosis
Bile acid metabolism
Cholesterol homeostasis
Coagulation
Complement
DNA repair
E2F targets
Epithelial mesenchymal transition
Estrogen response early
Estrogen response late
Fatty acid metabolism
G2M checkpoint
Glycolysis
Hedgehog signaling
Heme metabolism
Hypoxia
IL2 STAT5 signaling
IL6 JAK STAT3 signaling
Inflammatory response
Interferon alpha response
Interferon gamma response
KRAS signaling dn
KRAS signaling up
Mitotic spindle
MTORC1 signaling
MYC targets v1
MYC targets v2
Myogenesis
Notch signaling
Oxidative phosphorylation
P53 pathway
Pancreas beta cells
Peroxisome
PI3K Akt mtor signaling
Protein secretion
Reactive oxygen species pathway
Spermatogenesis
TGF Beta signaling
TNFA signaling via nfkb
Unfolded protein response
UV response dn
UV response up
WNT beta catenin signaling
Xenobiotic metabolism
HBCA
Basal
LumHR-major
LumHR-active
LumSec-major
LumSec-KIT
LumSec-HLA
LumHR-SCGB
LumSec-prol
LumSec-lac
LumSec-basal
LumSec-myo
Inf.CNV
Prop. Malignant
Patient
Grade 1 (7%)
Grade 2 (25%)
Grade 3 (68%)
ER+ (59%)
HER2+ (11%)
TNBC (25%)
Mean Age
13 2 4 5 0 22 6 8 15 18 3 16 1 17 14 20
Level 1
Level 2
Level 3
Scaled Scores
Proportions
Age
RF OOB Acc.
Cyto. Score
Basal (PAM50)
Epi. State
Basal (HBCA)
Lumsec-Basal (HBCA)
Age
Mes. State
Protein Secretion (Hall.)
Lumhr-Active (HBCA)
P53 Pathway (Hall.)
G2m Checkpoint (Hall.)
Mtorc1 Signaling (Hall.)
Myc Targets V1 (Hall.)
Lumsec-Kit (HBCA)
Oxidative Phosphorylation (Hall.)
Tnfa Signaling Via Nfkb (Hall.)
Lumsec-Myo (HBCA)
Epithelial Mesenchymal Transition (Hall.)
Myogenesis (Hall.)
Lumsec-Prol (HBCA)
Estrogen Response Early (Hall.)
LumA (PAM50)
Estrogen Response Late (Hall.)
E2f Targets (Hall.)
Her2 (PAM50)
Grade
Interferon Alpha Response (Hall.)
Int. State
Lumsec-Hla (HBCA)
Features
Scores
High
Low

Figure 4

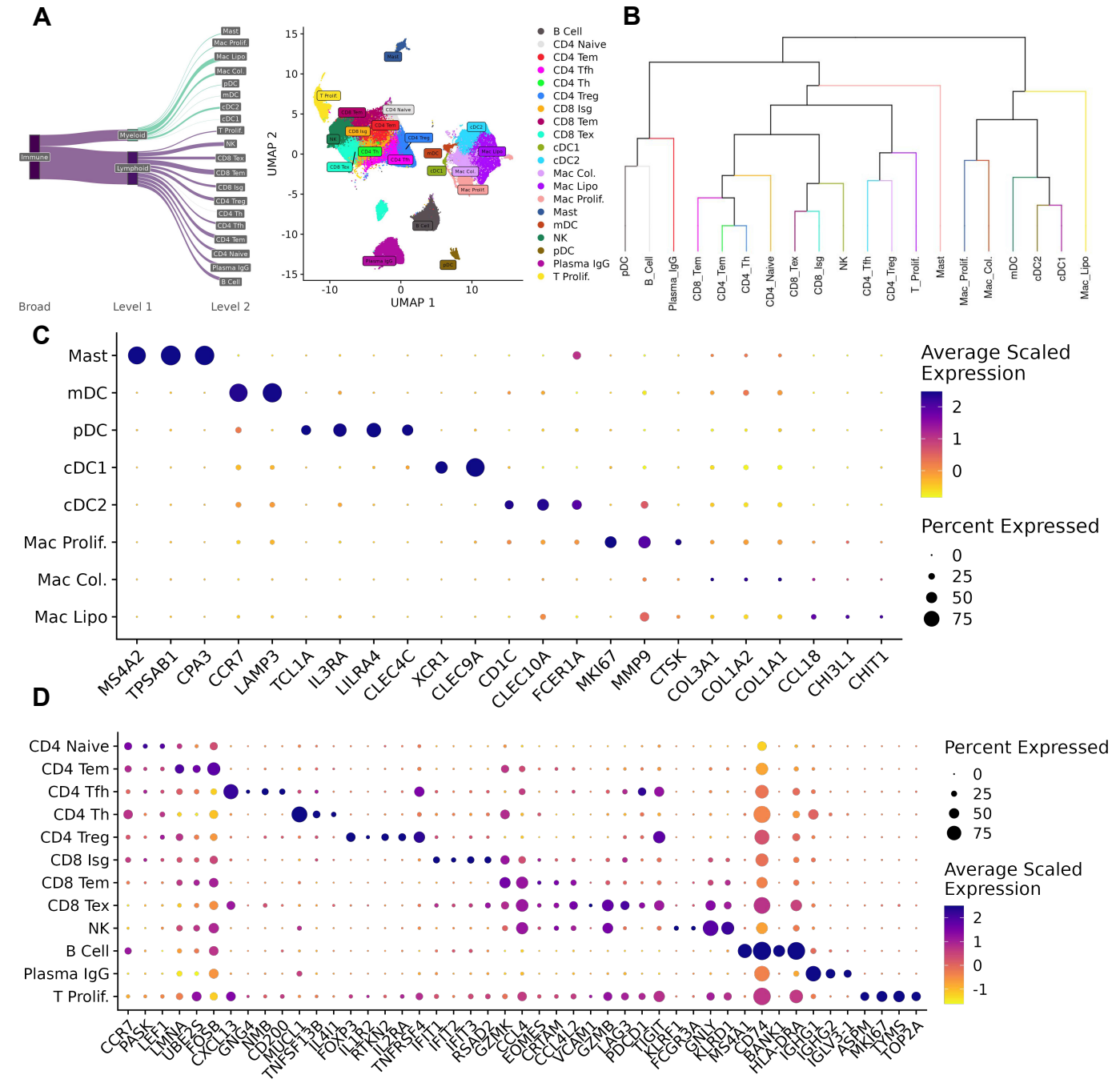
A
Broad
Level 1
Level 2
Immune
Myeloid
Lymphoid
Mast
Mac Prolif.
Mac Lipo
Mac Col.
pDC
mDC
cDC2
cDC1
T Prolif.
NK
CD8 Tex
CD8 Tem
CD8 Isg
CD4 Treg
CD4 Th
CD4 Tfh
CD4 Tem
CD4 Naive
Plasma IgG
B Cell
UMAP 1
UMAP 2
B Cell
CD4 Naive
CD4 Tem
CD4 Tfh
CD4 Th
CD4 Treg
CD8 Isg
CD8 Tem
CD8 Tex
cDC1
cDC2
Mac Col.
Mac Lipo
Mac Prolif.
Mast
mDC
NK
pDC
Plasma IgG
T Prolif.
B
pDC
B_Cell
Plasma_IgG
CD8_Tem
CD4_Tem
CD4_Th
CD4_Naive
CD8_Tex
CD8_Isg
NK
CD4_Tfh
CD4_Treg
T_Prolif.
Mast
Mac_Prolif.
Mac_Col.
mDC
cDC2
cDC1
Mac_Lipo
C
Mast
mDC
pDC
cDC1
cDC2
Mac Prolif.
Mac Col.
Mac Lipo
MS4A2
TPSAB1
CPA3
CCR7
LAMP3
TCL1A
IL3RA
LILRA4
CLEC4C
XCR1
CLEC9A
CD1C
CLEC10A
FCER1A
MKI67
MMP9
CTSK
COL3A1
COL1A2
COL1A1
CCL18
CHI3L1
CHIT1
Average Scaled Expression
2
1
0
Percent Expressed
0
25
50
75
D
CD4 Naive
CD4 Tem
CD4 Tfh
CD4 Th
CD4 Treg
CD8 Isg
CD8 Tem
CD8 Tex
NK
B Cell
Plasma IgG
T Prolif.
CCR7
PASK
LEF1
LMNA
UBE2S
FOSB
CXCL13
GNG4
NMB
CD200
MUC1
TNFSF13B
IL4I1
FOXP3
ILR2
RTKN2
IL2RA
TNFRSF4
IFIT1
IFIT2
IFIT3
RSAD2
GZMK
CCL4
EOMES
CRTAM
CCL4L2
VCAM1
GZMB
LAG3
PDCD1
TIGIT
KLRF1
FCGR3A
GNLY
KLRD1
MS4A1
CD74
BANK1
HLA-DRA
IGHG1
IGHG2
IGLV3-1
ASPM
MKI67
TYMS
TOP2A
Percent Expressed
0
25
50
75
Average Scaled Expression
2
1
0
-1

Figure 5

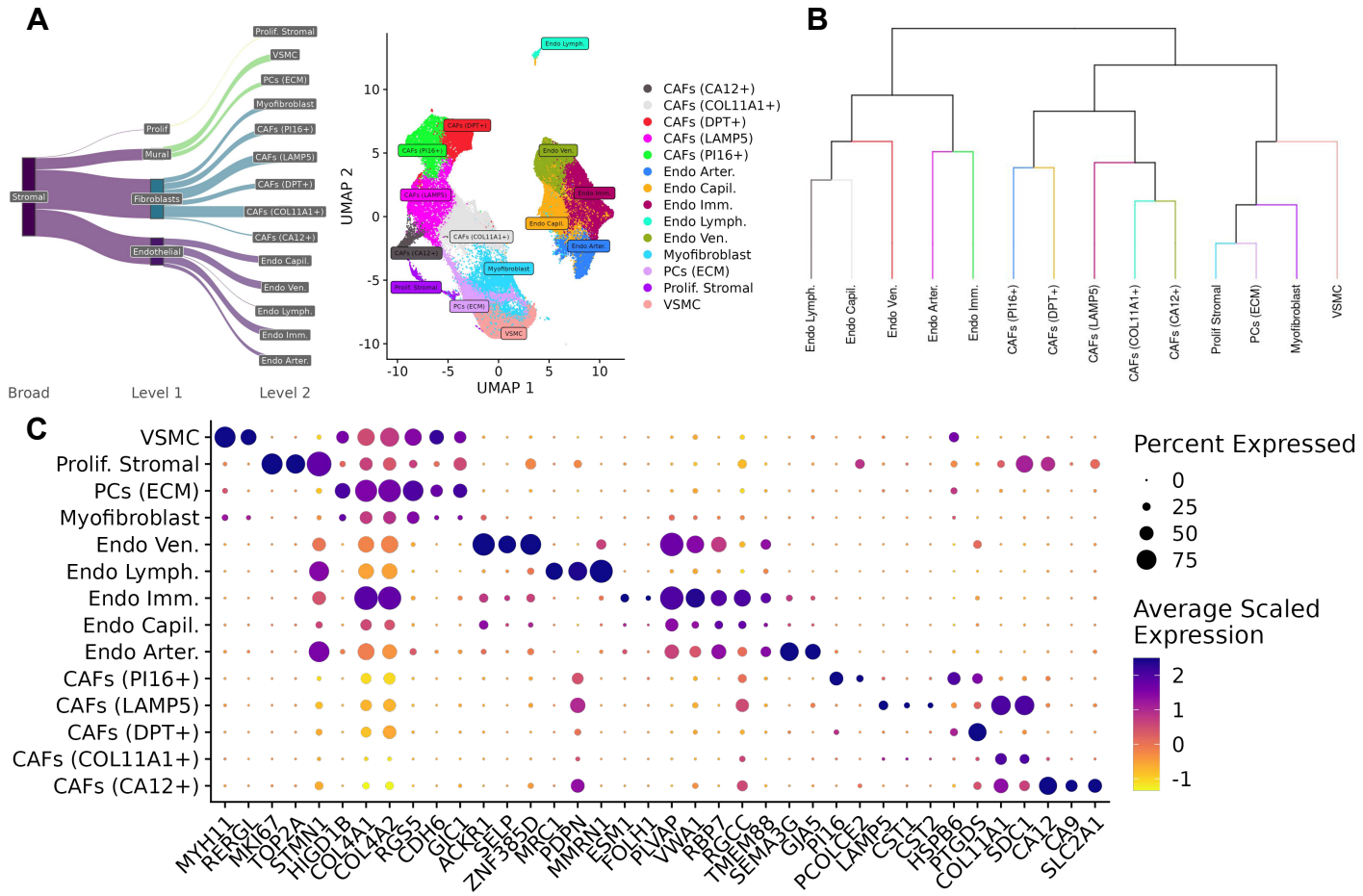
A
Broad
Level 1
Level 2
Stromal
Endothelial
Fibroblasts
Mural
Prolif
Prolif. Stromal
VSMC
PCs (ECM)
Myofibroblast
CAFs (PI16+)
CAFs (LAMP5)
CAFs (DPT+)
CAFs (COL11A1+)
CAFs (CA12+)
Endo Capil.
Endo Ven.
Endo Lymph.
Endo Imm.
Endo Arter.
UMAP 1
UMAP 2
CAFs (CA12+)
CAFs (COL11A1+)
CAFs (DPT+)
CAFs (LAMP5)
CAFs (PI16+)
Endo Arter.
Endo Capil.
Endo Imm.
Endo Lymph.
Endo Ven.
Myofibroblast
PCs (ECM)
Prolif. Stromal
VSMC
B
Endo Lymph.
Endo Capil.
Endo Ven.
Endo Arter.
Endo Imm.
CAFs (PI16+)
CAFs (DPT+)
CAFs (LAMP5)
CAFs (COL11A1+)
CAFs (CA12+)
Prolif Stromal
PCs (ECM)
Myofibroblast
VSMC
C
VSMC
Prolif. Stromal
PCs (ECM)
Myofibroblast
Endo Ven.
Endo Lymph.
Endo Imm.
Endo Capil.
Endo Arter.
CAFs (PI16+)
CAFs (LAMP5)
CAFs (DPT+)
CAFs (COL11A1+)
CAFs (CA12+)
MYH11
RERGL
MKI67
TOP2A
STMN1
HIGD1B
COL4A1
COL4A2
RGS5
CDH6
GJC1
ACKR1
SELP
ZNF385D
MRC1
PDPN
MMRN1
ESM1
FOLH1
PLVAP
VWA1
RBP7
RGCC
TMEM88
SEMA3G
GJA5
PI16
PCOLCE2
LAMP5
CST1
CST2
HSPB6
PTGDS
COL11A1
SDC1
CA12
CA9
SLC2A1
Percent Expressed
0
25
50
75
Average Scaled Expression
2
1
0
-1

Figure 6

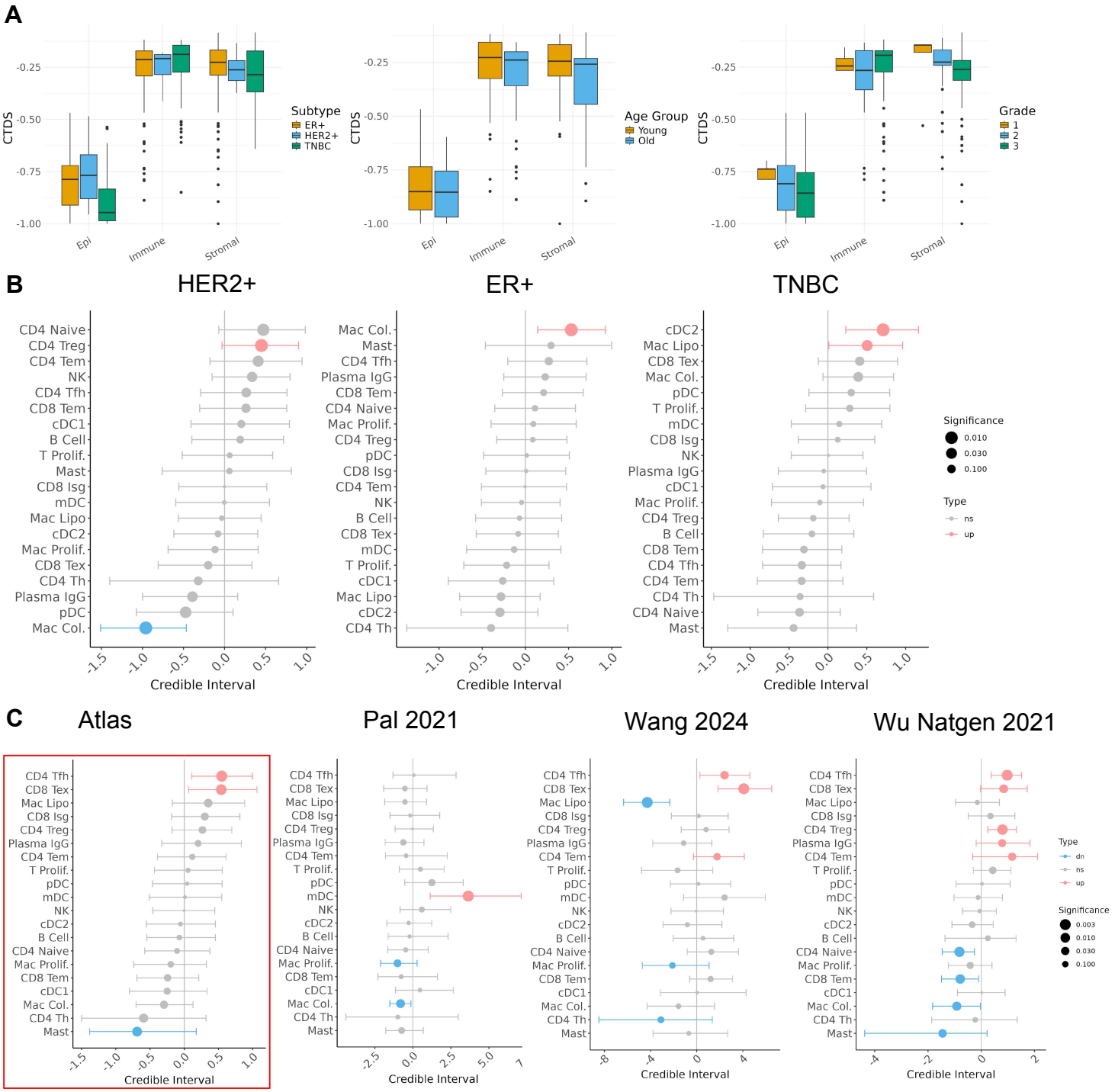
A
CTDS
Epi
Immune
Stromal
Subtype
ER+
HER2+
TNBC
Age Group
Young
Old
Grade
1
2
3
B
HER2+
ER+
TNBC
Credible Interval
Significance
0.010
0.030
0.100
Type
ns
up
C
Atlas
Pal 2021
Wang 2024
Wu Natgen 2021
Credible Interval
Type
dn
ns
up
Significance
0.003
0.010
0.030
0.100

Figure 7

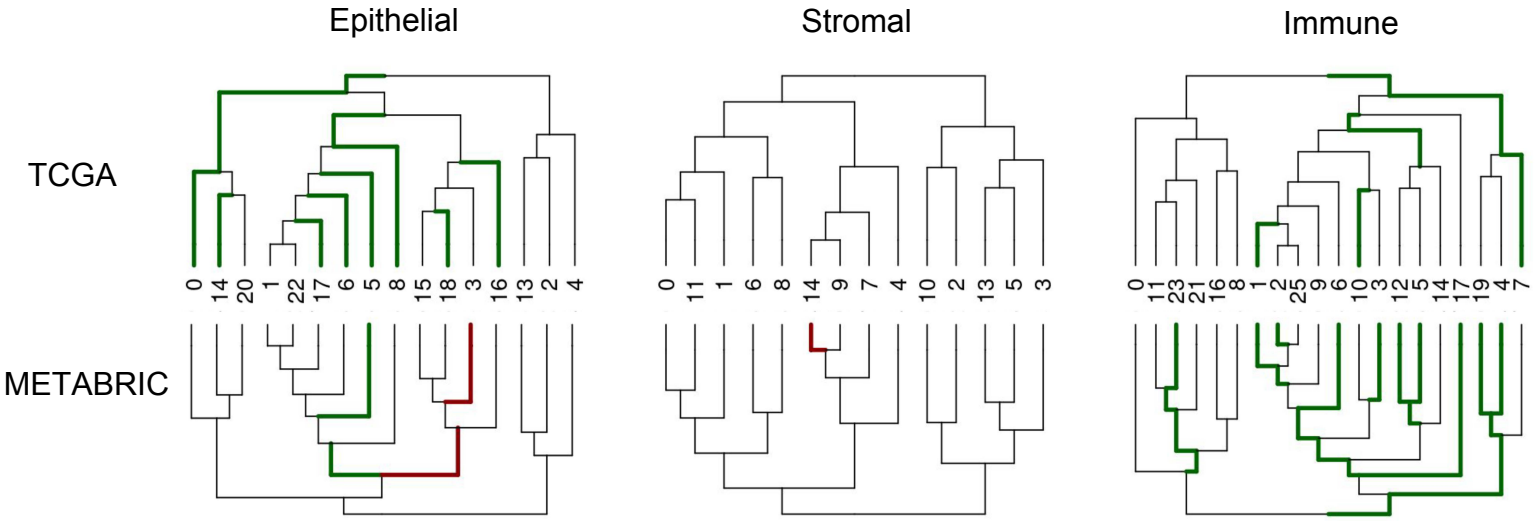
Epithelial
Stromal
Immune
TCGA
METABRIC
0 14 20 1 22 17 6 5 8 15 18 3 16 13 2 4
0 11 1 6 8 14 9 7 4 10 2 13 5 3
0 11 23 21 16 8 1 2 25 9 6 10 3 12 5 14 17 19 4 7

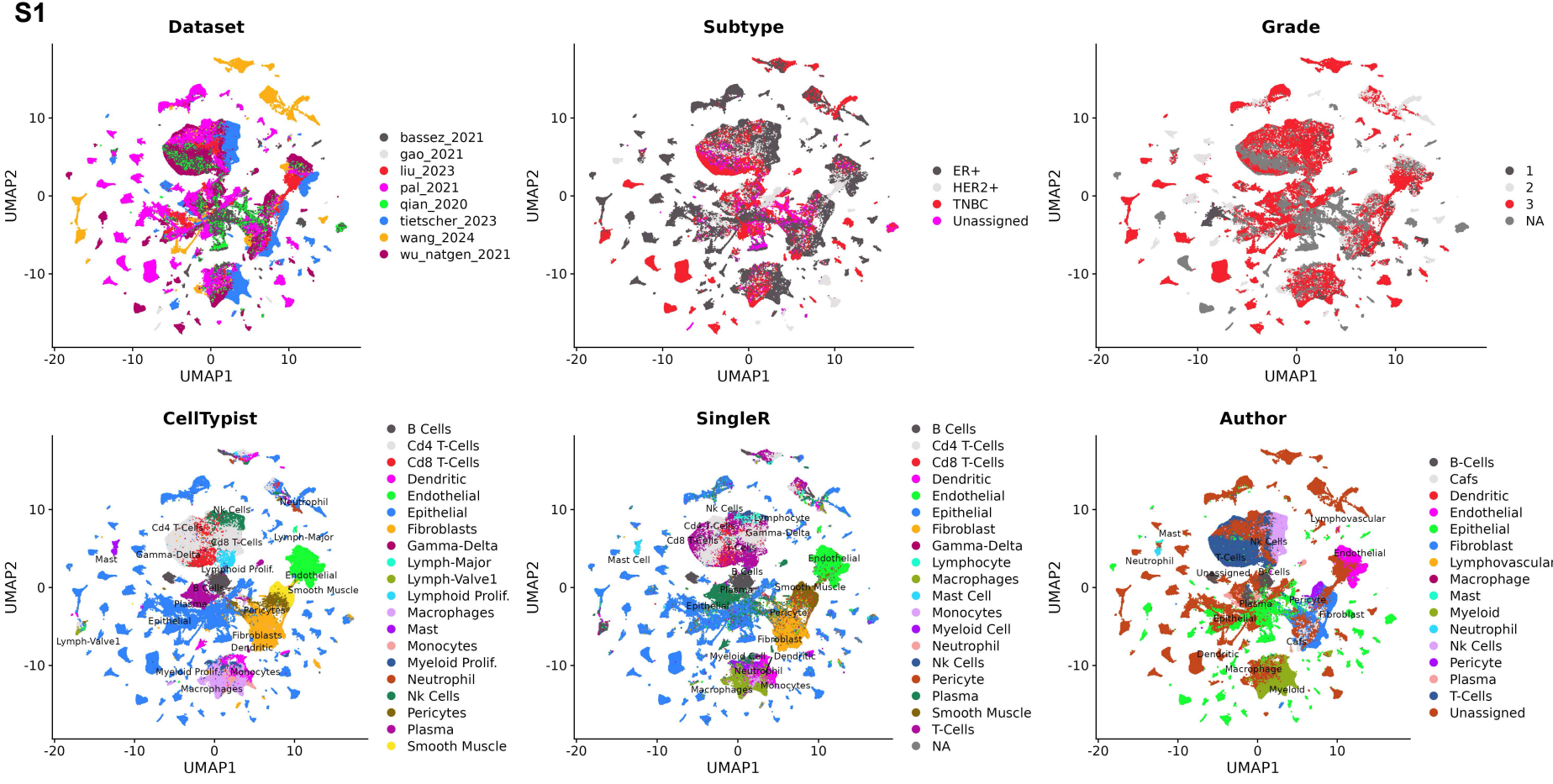
S1
Dataset
bassez_2021
gao_2021
liu_2023
pal_2021
qian_2020
tietscher_2023
wang_2024
wu_natgen_2021
Subtype
ER+
HER2+
TNBC
Unassigned
Grade
1
2
3
NA
CellTypist
B Cells
Cd4 T-Cells
Cd8 T-Cells
Dendritic
Endothelial
Epithelial
Fibroblasts
Gamma-Delta
Lymph-Major
Lymph-Valve1
Lymphoid Prolif.
Macrophages
Mast
Monocytes
Myeloid Prolif.
Neutrophil
Nk Cells
Pericytes
Plasma
Smooth Muscle
SingleR
B Cells
Cd4 T-Cells
Cd8 T-Cells
Dendritic
Endothelial
Epithelial
Fibroblast
Gamma-Delta
Lymphocyte
Macrophages
Mast Cell
Monocytes
Myeloid Cell
Neutrophil
Nk Cells
Pericyte
Plasma
Smooth Muscle
T-Cells
NA
Author
B-Cells
Cafs
Dendritic
Endothelial
Epithelial
Fibroblast
Lymphovascular
Macrophage
Mast
Myeloid
Neutrophil
Nk Cells
Pericyte
Plasma
T-Cells
Unassigned
UMAP1
UMAP2

S2

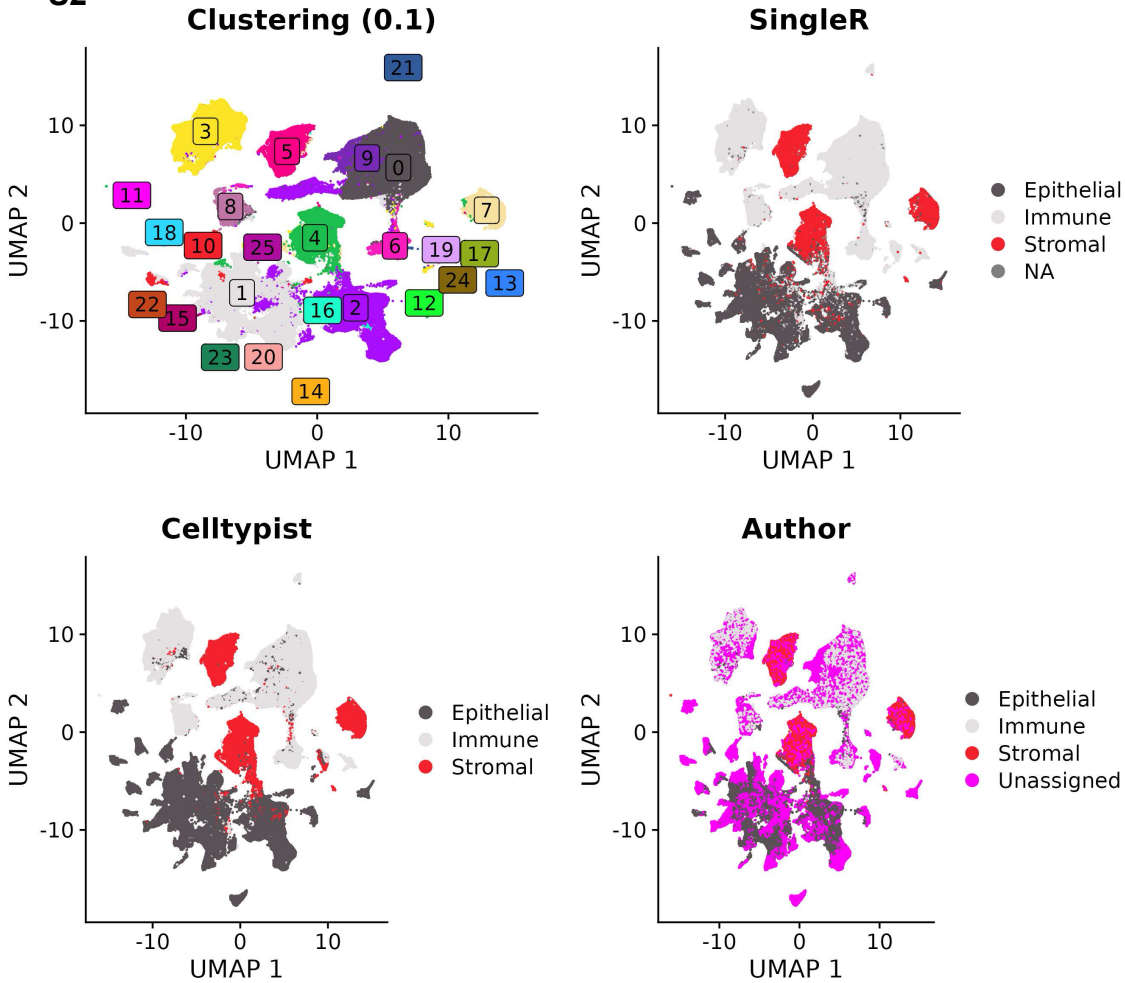
Clustering (0.1)
SingleR
Celltypist
Author
UMAP 1
UMAP 2
Epithelial
Immune
Stromal
NA
Unassigned

S3

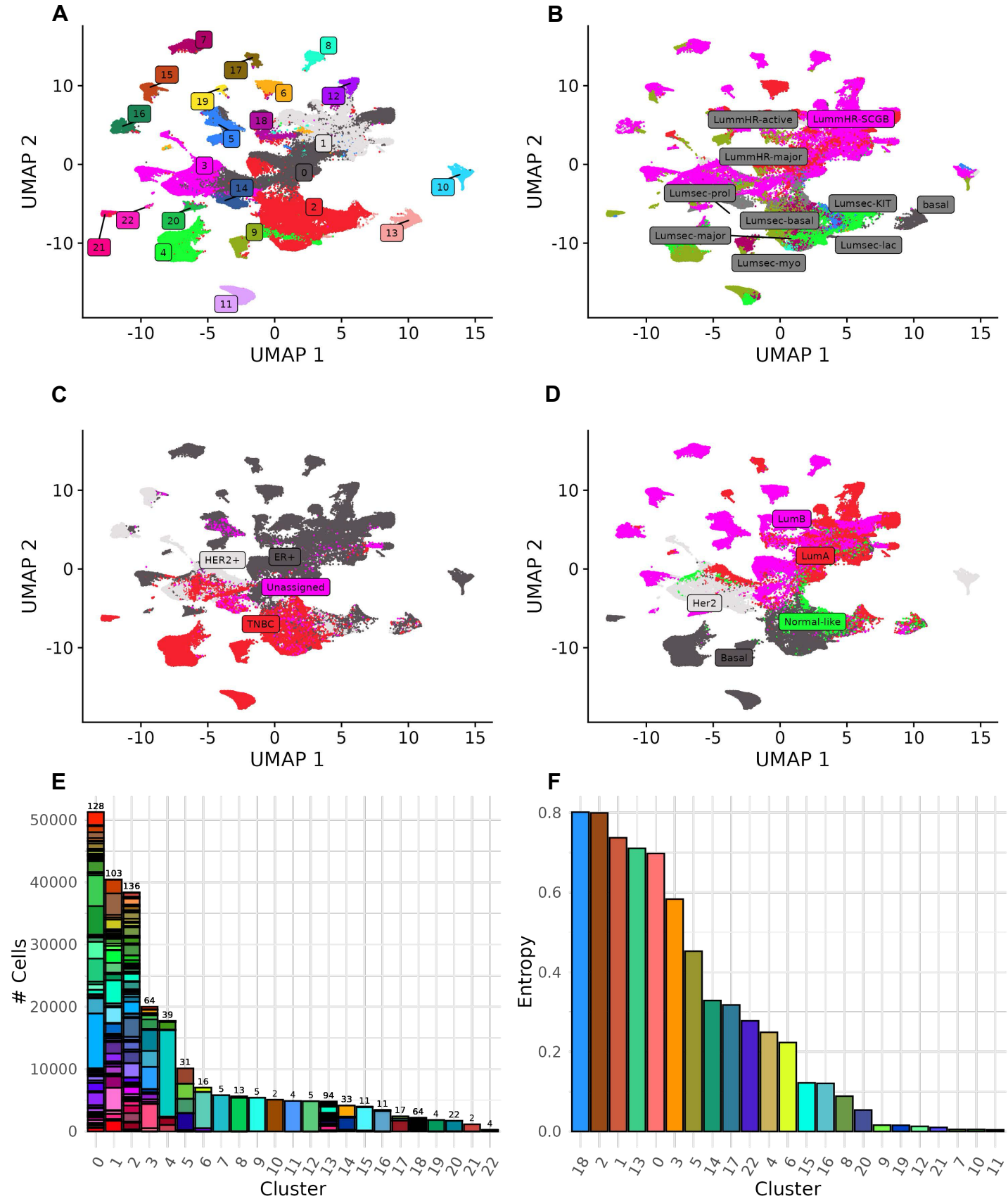
A
B
C
D
E
F
UMAP 1
UMAP 2
LummHR-active
LummHR-SCGB
LummHR-major
Lumsec-prol
Lumsec-KIT
basal
Lumsec-basal
Lumsec-major
Lumsec-lac
Lumsec-myo
HER2+
ER+
Unassigned
TNBC
LumB
LumA
Her2
Normal-like
Basal
Cells
Cluster
Entropy

S4

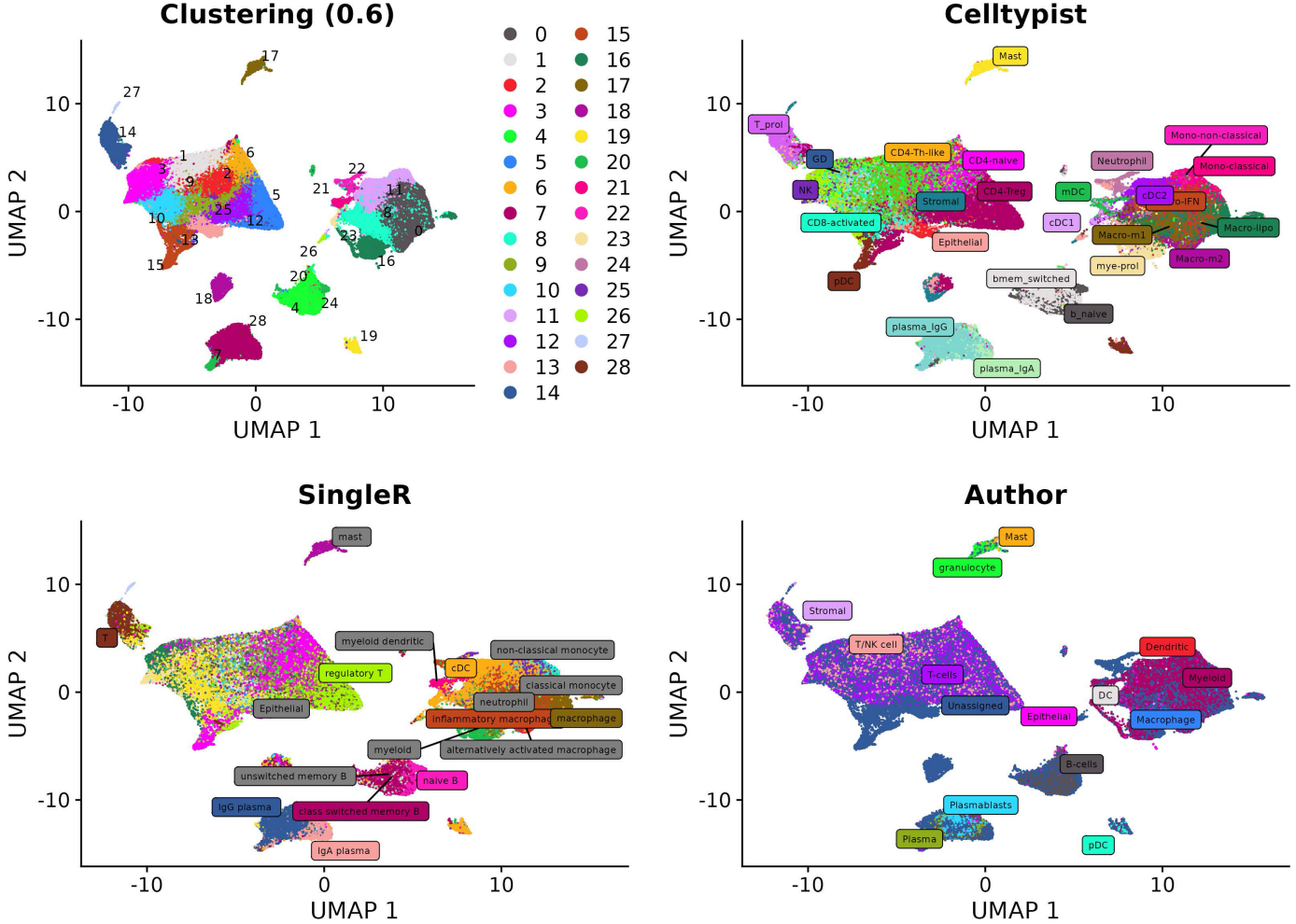
Clustering (0.6)
Celltypist
SingleR
Author
UMAP 1
UMAP 2
0 1 2 3 4 5 6 7 8 9 10 11 12 13 14 15 16 17 18 19 20 21 22 23 24 25 26 27 28
Mast
T_prol
GD
CD4-Th-like
CD4-naive
NK
Stromal
CD4-Treg
CD8-activated
Epithelial
pDC
bmem_switched
plasma_IgG
plasma_IgA
b_naive
Neutrophil
Mono-non-classical
Mono-classical
mDC
cDC2
o-IFN
cDC1
Macro-m1
Macro-lipo
Macro-m2
mye-prol
mast
myeloid dendritic
non-classical monocyte
cDC
regulatory T
classical monocyte
neutrophil
Epithelial
Inflammatory macrophag
macrophage
myeloid
alternatively activated macrophage
unswitched memory B
naive B
IgG plasma
class switched memory B
IgA plasma
Mast
granulocyte
Stromal
T/NK cell
Dendritic
T-cells
Myeloid
DC
Unassigned
Epithelial
Macrophage
B-cells
Plasmablasts
Plasma
pDC

S5

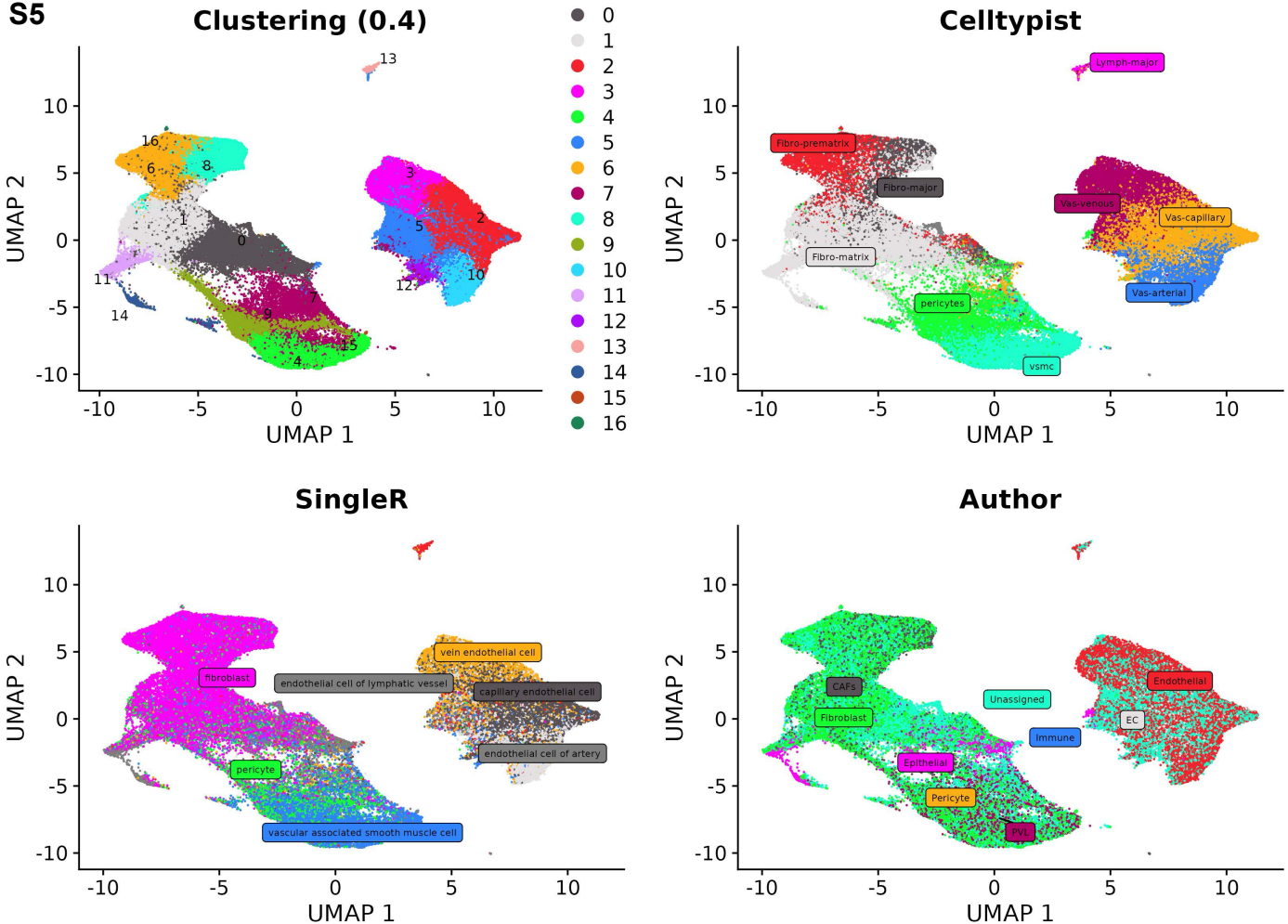
Clustering (0.4)
0
1
2
3
4
5
6
7
8
9
10
11
12
13
14
15
16
Celltypist
Lymph-major
Fibro-prematrix
Fibro-major
Fibro-matrix
Vas-venous
Vas-capillary
Vas-arterial
pericytes
vsmc
SingleR
fibroblast
endothelial cell of lymphatic vessel
vein endothelial cell
capillary endothelial cell
endothelial cell of artery
pericyte
vascular associated smooth muscle cell
Author
CAFs
Fibroblast
Unassigned
Endothelial
EC
Immune
Epithelial
Pericyte
PVL
UMAP 1
UMAP 2

S6

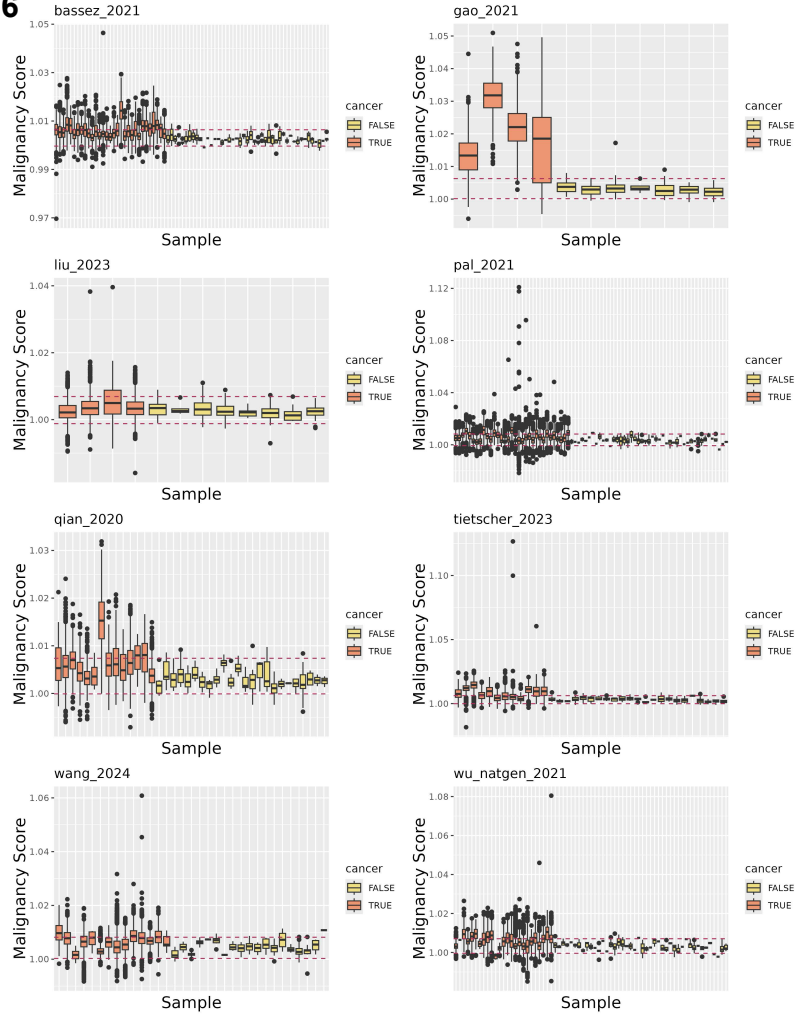
bassez_2021
gao_2021
liu_2023
pal_2021
qian_2020
tietscher_2023
wang_2024
wu_natgen_2021
Malignancy Score
Sample
cancer
FALSE
TRUE